The Astrophysical Journal Letters, 912:L27 (15pp), 2021 May 10 https://doi.org/10.3847/2041-8213/abeb1c

The JCMT BISTRO Survey: Revealing the Diverse Magnetic Field Morphologies in Taurus Dense Cores with Sensitive Submillimeter Polarimetry

Chakali Eswaraiah[1,90], Di Li[1,2,3], Ray S. Furuya[4], Tetsuo Hasegawa[5], Derek Ward-Thompson[6], Keping Qiu[7,8], Nagayoshi Ohashi[9], Kate Pattle[10], Sarah Sadavoy[11], Charles L. H. Hull[12,13,89], David Berry[14], Yasuo Doi[15], Tao-Chung Ching[1], Shih-Ping Lai[16,17], Jia-Wei Wang[17], Patrick M. Koch[9], Jungmi Kwon[18], Woojin Kwon[19,20], Pierre Bastien[21], Doris Arzoumanian[22], Simon Coudé[23], Archana Soam[23], Lapo Fanciullo[9], Hsi-Wei Yen[9], Junhao Liu[24,25], Thiem Hoang[26,27], Wen Ping Chen[28], Yoshito Shimajiri[5], Tie Liu[29], Zhiwei Chen[30], Hua-bai Li[31], A-Ran Lyo[26], Jihye Hwang[26,27], Doug Johnstone[32,33], Ramprasad Rao[9], Nguyen Bich Ngoc[34,35], Pham Ngoc Diep[34], Steve Mairs[14], Harriet Parsons[14], Motohide Tamura[5,18,36], Mehrnoosh Tahani[37], Huei-Ru Vivien Chen[9,16], Fumitaka Nakamura[38,39], Hiroko Shinnaga[40], Ya-Wen Tang[9], Jungyeon Cho[41], Chang Won Lee[26,27], Shu-ichiro Inutsuka[42], Tsuyoshi Inoue[42], Kazunari Iwasaki[43], Lei Qian[1], Jinjin Xie[1,2], Dalei Li[44], Hong-Li Liu[29,45,46], Chuan-Peng Zhang[1], Mike Chen[33], Guoyin Zhang[47], Lei Zhu[1], Jianjun Zhou[44], Philippe André[48], Sheng-Yuan Liu[9], Jinghua Yuan[1], Xing Lu[49], Nicolas Peretto[50], Tyler L. Bourke[51,52], Do-Young Byun[26,27], Sophia Dai[1], Yan Duan[1], Hao-Yuan Duan[16], David Eden[53], Brenda Matthews[32,33], Jason Fiege[54], Laura M. Fissel[11], Kee-Tae Kim[26,27], Chin-Fei Lee[9], Jongsoo Kim[26,27], Tae-Soo Pyo[39,55], Yunhee Choi[26], Minho Choi[26], Antonio Chrysostomou[51], Eun Jung Chung[41], Le Ngoc Tram[56], Erica Franzmann[54], Per Friberg[57], Rachel Friesen[57], Gary Fuller[58], Tim Gledhill[59], Sarah Graves[14], Jane Greaves[50], Matt Griffin[50], Qilao Gu[31], Ilseung Han[26,27], Jennifer Hatchell[60], Saeko Hayashi[55], Martin Houde[61], Koji Kawabata[62,63,64], Il-Gyo Jeong[26], Ji-hyun Kang[26], Sung-ju Kang[26], Miju Kang[26], Akimasa Kataoka[38], Francisca Kemper[9,65], Mark Rawlings[14], Jonathan Rawlings[66], Brendan Retter[50], John Richer[67,68], Andrew Rigby[50], Hiro Saito[69], Giorgio Savini[70], Anna Scaife[58], Masumichi Seta[71], Gwanjeong Kim[72], Kyoung Hee Kim[26], Mi-Ryang Kim[26], Florian Kirchschlager[66], Jason Kirk[73], Masato I. N. Kobayashi[74], Vera Konyves[73], Takayoshi Kusune[49], Kevin Lacaille[75,76], Chi-Yan Law[31,77], Sang-Sung Lee[26,27], Yong-Hee Lee[78], Masafumi Matsumura[79], Gerald Moriarty-Schieven[32], Tetsuya Nagata[80], Hiroyuki Nakanishi[40], Takashi Onaka[18,81], Geumsook Park[26], Xindi Tang[44], Kohji Tomisaka[38,39], Yusuke Tsukamoto[40], Serena Viti[82], Hongchi Wang[83], Anthony Whitworth[50], Hyunju Yoo[26], Hyeong-Sik Yun[78], Tetsuya Zenko[80], Yapeng Zhang[31], Ilse de Looze[82], C. Darren Dowell[84], Stewart Eyres[85], Sam Falle[86], Jean-François Robitaille[87], and Sven van Loo[88]

[1] National Astronomical Observatories, Chinese Academy of Sciences, A20 Datun Road, Chaoyang District, Beijing 100012, People's Republic of China eswaraiahc@nao.cas.cn, eswaraiahc@outlook.com
[2] University of Chinese Academy of Sciences, Beijing 100049, People's Republic of China; dili@nao.cas.cn
[3] NAOC-UKZN Computational Astrophysics Centre, University of KwaZulu-Natal, Durban 4000, South Africa
[4] Institute of Liberal Arts and Sciences, Tokushima University, Minami Jousanajima-machi 1-1, Tokushima 770-8502, Japan; rsf@tokushima-u.ac.jp
[5] National Astronomical Observatory of Japan, National Institutes of Natural Sciences, Osawa, Mitaka, Tokyo 181-8588, Japan
[6] Jeremiah Horrocks Institute, University of Central Lancashire, Preston PR1 2HE, UK
[7] School of Astronomy and Space Science, Nanjing University, 163 Xianlin Avenue, Nanjing 210023, People's Republic of China
[8] Key Laboratory of Modern Astronomy and Astrophysics (Nanjing University), Ministry of Education, Nanjing 210023, People's Republic of China
[9] Academia Sinica Institute of Astronomy and Astrophysics, No. 1, Sec. 4., Roosevelt Road, Taipei 10617, Taiwan
[10] Centre for Astronomy, School of Physics, National University of Ireland Galway, University Road, Galway, H91TK33, Ireland
[11] Department for Physics, Engineering Physics and Astrophysics, Queen's University, Kingston, ON, K7L 3N6, Canada
[12] National Astronomical Observatory of Japan, Alonso de Córdova 3788, Office 61B, 7630422, Vitacura, Santiago, Chile
[13] Joint ALMA Observatory, Alonso de Córdova 3107, Vitacura, Santiago, Chile
[14] East Asian Observatory, 660 North A'ohōkū Place, University Park, Hilo, HI 96720, USA
[15] Department of Earth Science and Astronomy, Graduate School of Arts and Sciences, The University of Tokyo, 3-8-1 Komaba, Meguro, Tokyo 153-8902, Japan
[16] Institute of Astronomy and Department of Physics, National Tsing Hua University, Hsinchu 30013, Taiwan
[17] Academia Sinica Institute of Astronomy and Astrophysics, P.O. Box 23-141, Taipei 10617, Taiwan
[18] Department of Astronomy, Graduate School of Science, The University of Tokyo, 7-3-1 Hongo, Bunkyo-ku, Tokyo 113-0033, Japan
[19] Department of Earth Science Education, Seoul National University (SNU), 1 Gwanak-ro, Gwanak-gu, Seoul 08826, Republic of Korea
[20] SNU Astronomy Research Center, Seoul National University, 1 Gwanak-ro, Gwanak-gu, Seoul 08826, Republic of Korea
[21] Centre de recherche en astrophysique du Québec & département de physique, Université de Montréal, 1375, Avenue Thérèse-Lavoie-Roux Montréal, QC, H2V 0B3, Canada
[22] Aix Marseille Univ, CNRS, CNES, LAM, Marseille, France
[23] SOFIA Science Center, Universities Space Research Association, NASA Ames Research Center, Moffett Field, CA 94035, USA
[24] School of Astronomy and Space Science, Nanjing University, 163 Xianlin Avenue, Nanjing 210023, People's Republic of China
[25] Key Laboratory of Modern Astronomy and Astrophysics (Nanjing University), Ministry of Education, Nanjing 210023, People's Republic of China
[26] Korea Astronomy and Space Science Institute, 776 Daedeokdae-ro, Yuseong-gu, Daejeon 34055, Republic of Korea
[27] University of Science and Technology, Korea, 217 Gajeong-ro, Yuseong-gu, Daejeon 34113, Republic of Korea
[28] Institute of Astronomy, National Central University, Zhongli 32001, Taiwan
[29] Shanghai Astronomical Observatory, Chinese Academy of Sciences, 80 Nandan Road, Shanghai 200030, People's Republic of China
[30] Purple Mountain Observatory and Key Laboratory of Radio Astronomy, Chinese Academy of Sciences, 2 West Beijing Road, Nanjing 210008, People's Republic of China
[31] Department of Physics, The Chinese University of Hong Kong, Shatin, N.T., Hong Kong
[32] NRC Herzberg Astronomy and Astrophysics, 5071 West Saanich Road, Victoria, BC V9E 2E7, Canada
[33] Department of Physics and Astronomy, University of Victoria, Victoria, BC V8W 2Y2, Canada

[34] Vietnam National Space Center, Vietnam Academy of Science and Technology, 18 Hoang Quoc Viet, Hanoi, Vietnam
[35] Graduate University of Science and Technology, Vietnam Academy of Science and Technology, 18 Hoang Quoc Viet, Hanoi, Vietnam
[36] Astrobiology Center, National Institutes of Natural Sciences, 2-21-1 Osawa, Mitaka, Tokyo 181-8588, Japan
[37] Dominion Radio Astrophysical Observatory, Herzberg Astronomy and Astrophysics Research Centre, National Research Council Canada, P.O. Box 248, Penticton, BC V2A 6J9, Canada
[38] Division of Theoretical Astronomy, National Astronomical Observatory of Japan, Mitaka, Tokyo 181-8588, Japan
[39] SOKENDAI (The Graduate University for Advanced Studies), Hayama, Kanagawa 240-0193, Japan
[40] Department of Physics and Astronomy, Graduate School of Science and Engineering, Kagoshima University, 1-21-35 Korimoto, Kagoshima, Kagoshima 890-0065, Japan
[41] Department of Astronomy and Space Science, Chungnam National University, 99 Daehak-ro, Yuseong-gu, Daejeon 34134, Republic of Korea
[42] Department of Physics, Graduate School of Science, Nagoya University, Furo-cho, Chikusa-ku, Nagoya 464-8602, Japan
[43] Department of Environmental Systems Science, Doshisha University, Tatara, Miyakodani 1-3, Kyotanabe, Kyoto 610-0394, Japan
[44] Xinjiang Astronomical Observatory, Chinese Academy of Sciences, 150 Science 1-Street, Urumqi 830011, Xinjiang, People's Republic of China
[45] Department of Astronomy, Yunnan University, Kunming, 650091, People's Republic of China
[46] Chinese Academy of Sciences, South America Center for Astrophysics, Camino El Observatorio #1515, Las Condes, Santiago, Chile
[47] CAS Key Laboratory of FAST, National Astronomical Observatories, Chinese Academy of Sciences, People's Republic of China
[48] Laboratoire AIM CEA/DSM-CNRS-Université Paris Diderot, IRFU/Service d'Astrophysique, CEA Saclay, F-91191 Gif-sur-Yvette, France
[49] National Astronomical Observatory of Japan, Mitaka, Tokyo 181-8588, Japan
[50] School of Physics and Astronomy, Cardiff University, The Parade, Cardiff, CF24 3AA, UK
[51] SKA Organisation, Jodrell Bank, Lower Withington, Macclesfield, SK11 9FT, UK
[52] Jodrell Bank Centre for Astrophysics, School of Physics and Astronomy, University of Manchester, Manchester, M13 9PL, UK
[53] Astrophysics Research Institute, Liverpool John Moores University, IC2, Liverpool Science Park, 146 Brownlow Hill, Liverpool, L3 5RF, UK
[54] Department of Physics and Astronomy, The University of Manitoba, Winnipeg, MB R3T 2N2, Canada
[55] Subaru Telescope, National Astronomical Observatory of Japan, 650 North A'ohōkū Place, Hilo, HI 96720, USA
[56] University of Science and Technology of Hanoi, Vietnam Academy of Science and Technology, 18 Hoang Quoc Viet, Hanoi, Vietnam
[57] National Radio Astronomy Observatory, 520 Edgemont Road, Charlottesville, VA 22903, USA
[58] Jodrell Bank Centre for Astrophysics, School of Physics and Astronomy, University of Manchester, Oxford Road, Manchester, M13 9PL, UK
[59] School of Physics, Astronomy & Mathematics, University of Hertfordshire, College Lane, Hatfield, Hertfordshire AL10 9AB, UK
[60] Physics and Astronomy, University of Exeter, Stocker Road, Exeter EX4 4QL, UK
[61] Department of Physics and Astronomy, The University of Western Ontario, 1151 Richmond Street, London N6A 3K7, Canada
[62] Hiroshima Astrophysical Science Center, Hiroshima University, Kagamiyama 1-3-1, Higashi-Hiroshima, Hiroshima 739-8526, Japan
[63] Department of Physics, Hiroshima University, Kagamiyama 1-3-1, Higashi-Hiroshima, Hiroshima 739-8526, Japan
[64] Core Research for Energetic Universe (CORE-U), Hiroshima University, Kagamiyama 1-3-1, Higashi-Hiroshima, Hiroshima 739-8526, Japan
[65] European Southern Observatory, Karl-Schwarzschild-Str. 2, D-85748 Garching, Germany
[66] Department of Physics and Astronomy, University College London, WC1E 6BT London, UK
[67] Astrophysics Group, Cavendish Laboratory, J.J. Thomson Avenue, Cambridge CB3 0HE, UK
[68] Kavli Institute for Cosmology, Institute of Astronomy, University of Cambridge, Madingley Road, Cambridge, CB3 0HA, UK
[69] Faculty of Pure and Applied Sciences, University of Tsukuba, 1-1-1 Tennodai, Tsukuba, Ibaraki 305-8577, Japan
[70] OSL, Physics & Astronomy Department, University College London, WC1E 6BT London, UK
[71] Department of Physics, School of Science and Technology, Kwansei Gakuin University, 2-1 Gakuen, Sanda, Hyogo 669-1337, Japan
[72] Nobeyama Radio Observatory, National Astronomical Observatory of Japan, National Institutes of Natural Sciences, Nobeyama, Minamimaki, Minamisaku, Nagano 384-1305, Japan
[73] Jeremiah Horrocks Institute, University of Central Lancashire, Preston PR1 2HE, UK
[74] Astronomical Institute, Graduate School of Science, Tohoku University, Aoba-ku, Sendai, Miyagi 980-8578, Japan
[75] Department of Physics and Astronomy, McMaster University, Hamilton, ON L8S 4M1, Canada
[76] Department of Physics and Atmospheric Science, Dalhousie University, Halifax B3H 4R2, Canada
[77] Department of Space, Earth & Environment, Chalmers University of Technology, SE-412 96 Gothenburg, Sweden
[78] School of Space Research, Kyung Hee University, 1732 Deogyeong-daero, Giheung-gu, Yongin-si, Gyeonggi-do 17104, Republic of Korea
[79] Faculty of Education & Center for Educational Development and Support, Kagawa University, Saiwai-cho 1-1, Takamatsu, Kagawa, 760-8522, Japan
[80] Department of Astronomy, Graduate School of Science, Kyoto University, Sakyo-ku, Kyoto 606-8502, Japan
[81] Department of Physics, Faculty of Science and Engineering, Meisei University, 2-1-1 Hodokubo, Hino, Tokyo 191-8506, Japan
[82] Physics & Astronomy Department, University College London, WC1E 6BT London, UK
[83] Purple Mountain Observatory, Chinese Academy of Sciences, 2 West Beijing Road, 210008 Nanjing, People's Republic of China
[84] Jet Propulsion Laboratory, M/S 169-506, 4800 Oak Grove Drive, Pasadena, CA 91109, USA
[85] University of South Wales, Pontypridd, CF37 1DL, UK
[86] Department of Applied Mathematics, University of Leeds, Woodhouse Lane, Leeds LS2 9JT, UK
[87] Univ. Grenoble Alpes, CNRS, IPAG, F-38000 Grenoble, France
[88] School of Physics and Astronomy, University of Leeds, Woodhouse Lane, Leeds LS2 9JT, UK
Received 2020 November 19; revised 2021 February 16; accepted 2021 February 18; published 2021 May 10

Abstract

We have obtained sensitive dust continuum polarization observations at 850 μm in the B213 region of Taurus using POL-2 on SCUBA-2 at the James Clerk Maxwell Telescope as part of the *B*-fields in STar-forming Region Observations (BISTRO) survey. These observations allow us to probe magnetic field (*B*-field) at high spatial resolution ($\sim$2000 au or $\sim$0.01 pc at 140 pc) in two protostellar cores (K04166 and K04169) and one prestellar

[89] NAOJ Fellow.
[90] FAST Fellow.

core (Miz-8b) that lie within the B213 filament. Using the Davis–Chandrasekhar–Fermi method, we estimate the *B*-field strengths in K04166, K04169, and Miz-8b to be 38 ± 14, 44 ± 16, and 12 ± 5 μG, respectively. These cores show distinct mean *B*-field orientations. The *B*-field in K04166 is well ordered and aligned parallel to the orientations of the core minor axis, outflows, core rotation axis, and large-scale uniform *B*-field, in accordance with magnetically regulated star formation via ambipolar diffusion taking place in K04166. The *B*-field in K04169 is found to be ordered but oriented nearly perpendicular to the core minor axis and large-scale *B*-field and not well correlated with other axes. In contrast, Miz-8b exhibits a disordered *B*-field that shows no preferred alignment with the core minor axis or large-scale field. We found that only one core, K04166, retains a memory of the large-scale uniform *B*-field. The other two cores, K04169 and Miz-8b, are decoupled from the large-scale field. Such a complex *B*-field configuration could be caused by gas inflow onto the filament, even in the presence of a substantial magnetic flux.

Unified Astronomy Thesaurus concepts: Dust continuum emission (412); Polarimetry (1278); Low mass stars (2050); Dense interstellar clouds (371); Interstellar magnetic fields (845)

1. Introduction

According to the filamentary paradigm of star formation, low-mass stars predominantly form in dense cores that are distributed in a chain-like fashion along gravitationally unstable filamentary clouds (Hartmann 2002; André et al. 2014; Tafalla & Hacar 2015; Marsh et al. 2016). The magnetic field (*B*-field) is important at all scales during this process (Shu et al. 1987; McKee & Ostriker 2007; Crutcher 2012; Ward-Thompson et al. 2020). Nevertheless, the interplay between the *B*-field, gravity, and turbulence in the formation of cores and their collapse to form stars is still a subject of investigation.

Studies of the *B*-field on cloud scales with Planck 850 μm low-resolution ($\sim 5'$ or $\sim$0.2 at 140 pc) polarization observations and optical and near-infrared (NIR) polarimetry of background stars have revealed that low-density gas striations are mostly aligned with the *B*-field, and high-density filamentary structures are oriented perpendicular to the *B*-field (Alves et al. 2008; Sugitani et al. 2010; Chapman et al. 2011; Planck Collaboration et al. 2016a; Wang et al. 2020). These observations imply that material can accumulate along field lines and aid in the assembly of dense structures perpendicular to the *B*-field as a result of gravitational collapse and/or converging flows (see Ballesteros-Paredes et al. 1999a; Hartmann et al. 2001; Soler & Hennebelle 2017).

If the large-scale, uniform *B*-field is inherited down to core scale (<0.1 pc), it governs not only the contraction, stability, and collapse of the core (Mestel & Spitzer 1956; Mouschovias & Spitzer 1976) but also the properties of the circumstellar disk by helping to remove angular momentum via magnetic braking (Mouschovias 1991; Allen et al. 2003; Li et al. 2014). According to the theory of isolated, low-mass star formation via ambipolar diffusion (Mouschovias 1991; Mouschovias et al. 2006), the gravitational collapse of a dense core is regulated by a strong, ordered *B*-field such that the core preferentially contracts along field lines. As a result, the core acquires an oblate-like structure over 10,000 au scales. After gaining sufficient mass via *B*-field-mediated contraction, the subcritical core initially becomes supercritical and eventually collapses under its own gravity. At this stage, the flux-freezing condition will no longer be valid due to efficient neutral-ion decoupling. As a result of this ambipolar diffusion, the *B*-field will acquire an hourglass morphology on protostellar envelope scales, <1000 au (e.g., Galli & Shu 1993; Girart et al. 2006; Stephens et al. 2013). This model predicts a positive correlation between the angle of the mean *B*-field and that of the minor axes of the filament and core and the axes of both pseudodisk symmetry and bipolar outflow (Fiedler & Mouschovias 1992, 1993; Galli & Shu 1993; Mocz et al. 2017; Hull & Zhang 2019).

Evidence for magnetically regulated star formation through observations of a coherent *B*-field across orders of magnitude in size scale (e.g., Li et al. 2006, 2009; Hull et al. 2014) is not always the norm. A departure from coherency, especially at smaller scales, can occur in regions dominated by turbulence (e.g., Hull et al. 2017b), shocks from outflows (e.g., Hull et al. 2017a), gravity-driven gas flows (e.g., Pillai et al. 2020), stellar feedback driven by expanding ionization fronts from H II regions (Arthur et al. 2011; Pattle et al. 2018; Eswaraiah et al. 2020), or gas dynamics arising from gravitational collapse (Ching et al. 2017, 2018). These observations suggest that the very local environment can determine the morphology and role of the *B*-field.

We emphasize here that *B*-field observations of low-mass dense cores (i) formed out of a single natal filament, (ii) characterized by an ordered *B*-field at larger scales (subparsec to several parsecs; see Figure 1(a)), (iii) having signposts of accretion flows (Palmeirim et al. 2013; Shimajiri et al. 2019), and (iv) hosting pristine physical conditions unaffected by any disruption by strong stellar feedback are sparse. Taurus B213 is one of these rare regions, making the B213 cores the ideal laboratories to understand the role of the *B*-field in the star formation process.

We conduct sensitive dust polarization observations at 850 μm toward B213 as part of the *B*-fields In STar-forming Region Observations (BISTRO; Ward-Thompson et al. 2017) survey to resolve its *B*-field. BISTRO is a large program on the 15 m James Clerk Maxwell Telescope (JCMT), making use of its SCUBA-2 camera and POL-2 polarimeter. The B213 filament is nearby (distance $\sim$140 pc; Elias 1978), well studied, and part of the $\sim$10 pc filament LDN 1495, as shown in Figure 1(a). It is fragmented into a chain of cores that are in the early evolutionary stages of low-mass star formation (Figure 1(b)). These include three prestellar cores, namely, Miz-8b, Miz-2, and HGBS-1 (Mizuno et al. 1994; Marsh et al. 2016); two class 0/I protostellar cores, IRAS 04166+2706 and IRAS 04169+2702 (Ohashi et al. 1997; Tafalla et al. 2010; Takakuwa et al. 2018); and one evolved object, J04194148+2716070, classified as a class II T Tauri star (Davis et al. 2010). We hereafter refer to IRAS 04166+2706 and IRAS 04169+2702 as K01466 and K04169, respectively (see Kenyon et al. 1990, 1993), adopting the core nomenclature of Bracco et al. (2017).

Here, for the first time, we resolve the *B*-field in the three cores of B213 on 0.01–0.1 pc spatial scales. In this letter, our key aims are to examine whether (i) *B*-fields at scales <0.1 pc are coherent with or decoupled from the uniform large-scale *B*-field and (ii) the paradigm of magnetically regulated, isolated

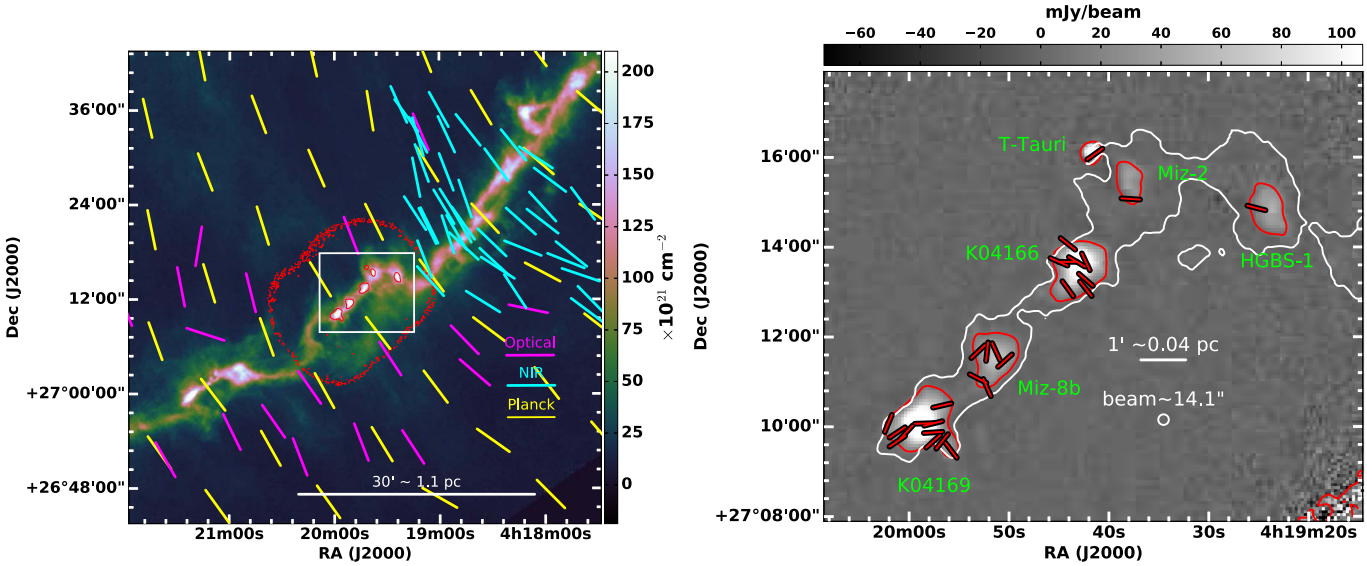

Figure 1. (a) The overall structure of the B213 filament is shown using a high-resolution (18.″2) column density map taken from the HGBS archive (Palmeirim et al. 2013). It is a part of the 10 pc long large-scale filament LDN 1495 in the Taurus molecular cloud. Measurements of the large-scale *B*-field orientation are overlaid: optical polarimetry measurements are shown as magenta segments (Heyer et al. 1987; Goodman et al. 1990; Heiles 2000), NIR polarimetry measurements as cyan segments (Goodman et al. 1992; Chapman et al. 2011), and Planck 850 μm dust emission polarimetry measurements as yellow segments. (b) Our inferred core-scale *B*-field geometry (red segments) superimposed on the area of our total intensity (Stokes *I*) map, which contains the fragmented cores of B213. The extent of the map is shown as a white box in panel (a). Plotted segments correspond to a detection at a minimum of 3σ in polarization fraction and 10σ in total intensity. Note that all segments are shown with equal lengths to better display the *B*-field morphology. The white contour marks a column density of 1×10^{22} cm^{-2} (Palmeirim et al. 2013), as measured in the Herschel data, that outlines the structure of the parental B213 filament, which has fragmented into the cores shown. Red contours in both panels mark 10σ total intensity (Stokes *I*) values, where $1\sigma = 1.3$ mJy beam^{-1} is the rms noise. Note that the apparent $>10\sigma$ intensity values seen in low column density regions in panel (a) result from low exposure times at the edges of the POL-2 map and so delineate the extent of our mapped area. Reference scale and beam size (~14.″1) are shown.

low-mass star formation holds in these cores. This paper is organized as follows. Section 2 describes the observations and data reduction. Sections 3 and 4 present the results and discussion, respectively, and Section 5 summarizes our main findings.

2. Observations and Data Reduction

The POL-2 observations of two fields in B213 were carried out as part of the JCMT BISTRO survey (JCMT project code M16AL004) between 2017 November 5 and 2019 January 8. The two fields, shown in Figure A2, have a center-to-center angular separation of ~5′ . The fields were each observed 20 times using the POL-2 DAISY mapping mode (Holland et al. 2013; Friberg et al. 2016). This mode results in maps with a 12′ diameter, of which the central ~7′ represents usable coverage, so these two pointings represent a tightly spaced mosaic. The observations were made in JCMT weather bands 1 and 2, with 225 GHz atmospheric opacity (τ_{225}) varying between 0.02 and 0.06. The total exposure time for the two fields is ~28 hr (14 hr in each of the two overlapping fields), resulting in one of the deepest observations yet made by the BISTRO survey.

The 850 μm POL-2 data were reduced using the pol2map routine recently added to SMURF (Berry et al. 2005; Chapin et al. 2013).[91] The final mosaicked maps, calibrated in millijanskys per beam, are produced from coadded Stokes *I*, *Q*, and *U* maps with a pixel size of 4″, while the final debiased polarization vector catalog is binned to 12″ to achieve better sensitivity. The rms noise values in our Stokes *I*, *Q*, *U*, and PI maps, binned to a pixel size of 12″, are ~1.3, ~0.9, ~0.9, and ~1.0 mJy beam^{-1}, respectively. Here PI represents the polarized intensity of the dust emission, debiased using the asymptotic estimator method; our PI map is shown in Figure A2. The instrumental polarization (IP) of POL-2 was corrected for using the "2019 August" IP model (Friberg et al. 2018). The POL-2 data reduction process is described in detail by Doi et al. (2020) and Pattle et al. (2021).

[91] http://starlink.eao.hawaii.edu/docs/sun258.htx/sun258ss73.html

3. Results

3.1. B-field on Small Scales

We present the data of 28 polarization measurements satisfying the following criteria: (i) the ratio of intensity to its uncertainty $I/\sigma_I > 10$ and (ii) the degree of polarization to its uncertainty $P/\sigma_P > 3$, where $P = \mathrm{PI}/I$. These measurements are listed in Table 1. The resulting PI within the core boundaries (see Appendix A) ranges from ~2 to ~4 mJy beam^{-1} with a median uncertainty in PI, σ_{PI}, of 0.64 mJy beam^{-1}. The polarization fraction ranges from ~0.8% to ~18% with a median value of ~7%. The B213 cores are characterized by weak dust emission (~12–318 mJy beam^{-1}), as well as weak polarized emission in comparison to the other regions studied by the BISTRO program (Ward-Thompson et al. 2017; Kwon et al. 2018; Soam et al. 2018; Coudé et al. 2019; Liu et al. 2019; Pattle et al. 2019; Wang et al. 2019; Doi et al. 2020).

Assuming a distance to Taurus of 140 pc, our observations allow us to delineate the *B*-field in B213 on scales ranging from ~2000 au (~0.01 pc) up to ~0.25 pc, the length over which the cores K04166, Miz-8b, and K04169 are distributed. The resulting *B*-field geometry, based on the 28 polarization measurements (see Table 1), is shown in Figure 1(b). Since the three cores, T Tauri,

Table 1
Polarization Data along with the Celestial Coordinates of the Pixels

R.A. (J2000) (deg) (1)	Decl. (J2000) (deg) (2)	$I \pm \sigma_I$ (mJy beam^{-1}) (3)	$Q \pm \sigma_Q$ (mJy beam^{-1}) (4)	$U \pm \sigma_U$ (mJy beam^{-1}) (5)	PI $\pm \sigma_{\rm PI}$ (mJy beam^{-1}) (6)	$P \pm \sigma_P$ (%) (7)	$\theta_{{\rm core},B} \pm \sigma_{\theta_{{\rm core},B}}$ (deg) (8)
64.982471	27.157917	25.0 ± 0.6	−0.7 ± 0.6	−2.5 ± 0.7	2.5 ± 0.7	9.8 ± 2.8	37 ± 7
65.004946	27.161250	16.9 ± 0.7	1.1 ± 0.7	2.7 ± 0.7	2.8 ± 0.7	16.8 ± 4.4	124 ± 7
64.989963	27.161250	33.0 ± 0.7	0.3 ± 0.6	3.0 ± 0.6	3.0 ± 0.6	9.0 ± 1.9	132 ± 6
64.986217	27.161250	37.3 ± 0.7	−0.7 ± 0.6	3.1 ± 0.7	3.1 ± 0.7	8.3 ± 1.8	141 ± 5
65.004946	27.164583	35.7 ± 0.7	1.1 ± 0.7	2.7 ± 0.7	2.9 ± 0.7	8.1 ± 1.9	124 ± 7
65.001200	27.164583	78.6 ± 0.7	−0.2 ± 0.7	2.7 ± 0.7	2.6 ± 0.7	3.3 ± 0.9	137 ± 7
64.989963	27.164583	113.9 ± 0.9	2.3 ± 0.6	0.3 ± 0.6	2.2 ± 0.6	1.9 ± 0.5	94 ± 8
65.008696	27.167917	20.3 ± 0.6	−1.6 ± 0.7	1.6 ± 0.7	2.2 ± 0.7	10.8 ± 3.3	157 ± 8
64.993708	27.167917	318.4 ± 1.7	2.7 ± 0.7	0.2 ± 0.6	2.6 ± 0.7	0.8 ± 0.2	92 ± 7
64.989963	27.167917	140.9 ± 0.8	3.1 ± 0.6	1.6 ± 0.6	3.5 ± 0.6	2.5 ± 0.4	104 ± 5
64.986212	27.174583	45.4 ± 0.6	1.9 ± 0.6	0.9 ± 0.6	2.0 ± 0.6	4.4 ± 1.3	103 ± 8
64.967479	27.181247	12.2 ± 0.5	−1.5 ± 0.6	−1.6 ± 0.6	2.1 ± 0.6	17.6 ± 5.1	24 ± 8
64.971225	27.184581	15.8 ± 0.6	1.4 ± 0.6	−1.9 ± 0.7	2.3 ± 0.6	14.4 ± 4.0	63 ± 7
64.959979	27.191247	46.1 ± 0.6	0.2 ± 0.6	2.0 ± 0.6	1.9 ± 0.6	4.1 ± 1.3	132 ± 9
64.971221	27.194583	26.1 ± 0.6	0.2 ± 0.6	2.9 ± 0.6	2.9 ± 0.6	11.0 ± 2.5	133 ± 6
64.967475	27.194581	48.4 ± 0.6	−2.0 ± 0.6	0.4 ± 0.6	1.9 ± 0.6	4.0 ± 1.3	174 ± 9
64.963729	27.194581	58.6 ± 0.6	−1.5 ± 0.6	−1.8 ± 0.6	2.3 ± 0.6	3.8 ± 1.0	25 ± 7
64.933733	27.217906	54.7 ± 0.6	−0.8 ± 0.6	−2.4 ± 0.6	2.5 ± 0.6	4.6 ± 1.1	36 ± 6
64.926237	27.217903	25.0 ± 0.6	−0.6 ± 0.5	−2.7 ± 0.7	2.7 ± 0.7	10.8 ± 2.7	39 ± 6
64.926237	27.221236	72.0 ± 0.6	0.4 ± 0.6	−2.9 ± 0.6	2.8 ± 0.6	3.9 ± 0.8	49 ± 6
64.937479	27.227906	37.7 ± 0.6	1.8 ± 0.6	−1.9 ± 0.7	2.5 ± 0.6	6.7 ± 1.7	66 ± 7
64.933729	27.227906	113.4 ± 0.7	2.2 ± 0.6	−0.0 ± 0.7	2.1 ± 0.6	1.8 ± 0.6	90 ± 9
64.929979	27.227903	290.0 ± 1.4	1.2 ± 0.6	−2.3 ± 0.6	2.5 ± 0.6	0.9 ± 0.2	59 ± 7
64.926233	27.227903	253.9 ± 1.5	−1.8 ± 0.6	−2.2 ± 0.7	2.8 ± 0.6	1.1 ± 0.3	25 ± 6
64.933725	27.234572	14.6 ± 0.6	0.5 ± 0.7	−2.2 ± 0.7	2.2 ± 0.7	14.9 ± 4.5	51 ± 9
64.854983	27.247850	29.3 ± 1.1	3.6 ± 1.0	−2.0 ± 1.0	3.9 ± 1.0	13.4 ± 3.5	76 ± 7
64.907471	27.251225	22.1 ± 0.8	4.0 ± 0.8	−0.5 ± 0.8	3.9 ± 0.8	17.8 ± 3.8	86 ± 6
64.922458	27.267900	91.9 ± 1.3	1.3 ± 0.9	3.7 ± 0.9	3.8 ± 0.9	4.2 ± 1.0	125 ± 7

Note. R.A. and decl: celestial coordinates. I: total intensity. Q and U: Stokes parameters. PI: debiased polarized intensity. P: debiased degree of polarization. $\theta_{{\rm core},B}$: B-field orientation, determined by applying an offset of 90° to the polarization angle.

Miz-2, and HGBS-1, have only a single measurement each (and also because the background noise dominates at the locations of these cores; see Appendix A), we exclude them from further analysis and discussion. The overall B-field morphology appears to be uniform within K04166 and K04169, but the mean field directions are offset by ∼90° from one another. In contrast, the B-field morphology in Miz-8b is complex.

We compute the weighted mean position angle (PA) of the core B-field, $\bar{\theta}_{{\rm core},B}$, using uncertainties in polarization angle as weights. These values are given in Table 2. The $\bar{\theta}_{{\rm core},B}$, along with the low-resolution B-field morphology based on Planck 850 μm polarization data, is shown in Figure 2. Table 2 lists the offset between $\bar{\theta}_{{\rm core},B}$ and the large-scale mean B-field orientation ($\theta_B^{\rm largescale}$; see Appendix B) based on multiwavelength polarimetry. Also listed are the offset between $\bar{\theta}_{{\rm core},B}$ and the PA of each core's major axis ($\theta_{\rm core}$; see Appendix C).

Interestingly, we see completely different B-field geometry in each of the three cores. The B-field in K04166 lies roughly parallel to the large-scale field (or perpendicular to the filament), while that in K04169 lies roughly perpendicular to the large-scale field (or roughly parallel to the filament). The field direction in Miz-8b lies roughly halfway between the other two, albeit with a larger standard deviation in B-field orientations (35°; see Table 2). Hence, we see that the core-scale B-field, in a set of cores spanning ∼6′, or ∼0.25 pc, appears to be rather complex.

Furthermore, we observe a good alignment between the core B-field (∼48°) and outflows (∼33°) in K04166 (Figures 2 and 3(d)), consistent with studies by Davidson et al. (2011) and Chapman et al. (2011). In contrast, we see a misalignment between the core mean B-field (∼121°) and the outflows (∼58°) in K04169 (Figures 2 and 3(e)), in accordance with studies by Hull et al. (2013, 2014), Hull & Zhang (2019), and Yen et al. (2021). Despite the fact that these two cores lie within ∼0.25 pc of each other, they exhibit different B-field/outflow orientations.

3.2. B-field Strength

Based on the assumption that turbulence-induced Alfvén waves can distort B-field orientations, the plane-of-the-sky component of the B-field strength ($B_{\rm pos}$) can be estimated using the Davis–Chandrasekhar–Fermi relation (DCF method; Davis 1951; Chandrasekhar & Fermi 1953),

$$B_{\rm pos} \simeq Q\sqrt{4\pi\ \mu m_{\rm H}\ n_{\rm H_2}}\left(\frac{\delta_{V_{\rm NT}}}{\delta_\theta}\right), \quad (1)$$

where $n_{\rm H_2}$ is the gas number density, $\delta_{V_{\rm NT}}$ is the nonthermal gas velocity dispersion, and δ_θ is the dispersion in polarization angles about the mean B-field orientation. Here Q is a factor accounting for line-of-sight and beam dilution effects, which we take as 0.5 based on studies using synthetic polarization maps generated from numerically simulated clouds (Ostriker et al. 2001). This suggests

Table 2
Various Parameters for K04166, K04169, and Miz-8b

No.	Parameter	K04166	K04169	Miz-8b
	Weighted Mean *B*-field Orientation along with Various Offset PAs			
1	No. of *B*-field segments	8	10	4
2	Weighted mean *B*-field orientation ($\bar{\theta}_{\mathrm{core},B} \pm \epsilon_{\bar{\theta}_{\mathrm{core},B}}$; deg)[a,b]	48 ± 2	121 ± 2	158 ± 4
3	Angular dispersion (δ_θ; deg)	18 ± 4	20 ± 3	35 ± 7
4	Standard deviation in $\theta_{\mathrm{core},B}$(deg)[b]	20	33	35
5	PA of core major axis (θ_{core}; deg)[c]	127 ± 20	126 ± 16	119 ± 30
6	$\lvert\bar{\theta}_{\mathrm{core},B} - \theta_B^{\mathrm{largescale}}\rvert$ (deg)[d]	19	88	51
7	$\lvert\bar{\theta}_{\mathrm{core},B} - \theta_{\mathrm{core}}\rvert$ (deg)	79	5	39
	Core Dimensions, Mass, Column and Number Densities, etc.			
1	Semimajor axis (a) (pc)	0.032 ± 0.005	0.036 ± 0.006	0.029 ± 0.010
2	Semiminor axis (b) (pc)	0.024 ± 0.003	0.025 ± 0.005	0.023 ± 0.005
3	Effective radius (R_{eff}) (pc)[e]	0.028 ± 0.003	0.030 ± 0.004	0.026 ± 0.005
4	Median dust temperature (T_{d}) (K)[f]	12.2 ± 0.4	12.2 ± 0.8	10.9 ± 0.2
5	Integrated flux (F_ν) (mJy)	1564	1969	516
6	Mass (M) ($M_\odot$)	0.55 ± 0.28	0.69 ± 0.36	0.22 ± 0.11
7	Column density ($N(\mathrm{H_2})$) $\times 10^{21}$ ($\mathrm{cm^{-2}}$)	10 ± 6	11 ± 6	5 ± 3
8	Number density ($n(\mathrm{H_2})$) $\times 10^4$ ($\mathrm{cm^{-3}}$)	9 ± 5	9 ± 6	5 ± 4
	B-field Strength and Magnetic and Turbulent Pressures, etc.			
1	*B*-field strength (using DCF method) (μG)	38 ± 14	44 ± 16	12 ± 5
2	*B*-field pressure (P_B; $\times 10^{-10}$ dyn $\mathrm{cm^{-2}}$)	0.6 ± 0.4	0.8 ± 0.6	0.06 ± 0.05
3	Turbulent pressure (P_{turb}; $\times 10^{-10}$ dyn $\mathrm{cm^{-2}}$)	0.4 ± 0.3	0.7 ± 0.5	0.2 ± 0.1
4	P_B/P_{turb}	1.3 ± 1.3	1.0 ± 1.0	0.3 ± 0.4
5	Mass-to-flux ratio criticality ($\lambda = (M/\phi)/(M/\phi)_{\mathrm{cri}}$)	0.7 ± 0.4	1.4 ± 1.0	3 ± 2
6	Alfvén velocity (V_{A}; km $\mathrm{s^{-1}}$)	0.17 ± 0.09	0.21 ± 0.12	0.07 ± 0.04
7	Alfvénic Mach number (M_{A})	1.1 ± 0.6	1.2 ± 0.7	2 ± 1
	Energy Parameters			
1	p	0.27	0.27	0.27
2	Rotational energy E_{rot} ($\times 10^{41}$ erg)	0.02	0.1	0.01
3	Magnetic energy E_{mag} ($\times 10^{41}$ erg)	2	3	0.1
4	$E_{\mathrm{rot}}/E_{\mathrm{mag}}$	0.01	0.04	0.05
	Various PAs			
1	Core minor axis PA (deg)	$\sim$37	$\sim$36	$\sim$29
2	Outflow PA (deg)[g]	$\sim$33	$\sim$58	...
3	Core θ_{G} (deg; from W to N)[h]	-169	-144	93
4	Core θ_{G} (deg; from N to E)[i]	101	126	3
5	PA of the core rotation axis (deg; from N to E)[i]	11	36	93

Notes.
[a] While estimating $\bar{\theta}_{\mathrm{core},B}$, one *B*-field segment associated with K04169, with PA $\sim 37°$, was ignored, as it belongs to an another condensation to the south of K04169. Similarly, two segments associated with Miz-8b, with PAs of 24° and 63°, were ignored, as they fall in the core boundary and do not represent the *B*-field orientation in Miz-8b. These ignored segments are, within 30°, parallel to the large-scale *B*-field (with a PA of 29°).
[b] We also cross-check the $\bar{\theta}_{\mathrm{core},B}$ and corresponding standard deviation values against the circular mean and circular standard deviation values (Doi et al. 2020; see their Appendix C), which are estimated to be $51° \pm 19°$, $121° \pm 21°$, and $158° \pm 35°$ for K04166, K04169, and Miz-8b, respectively. These values are quite consistent with the quoted weighted mean and standard deviations.
[c] Here θ_{core} is the PA of the major axis of the core obtained by fitting an ellipse to the 13 mJy $\mathrm{beam^{-1}}$ POL-2 Stokes *I* contours of the cores.
[d] Here $\theta_B^{\mathrm{largescale}}$ is the mean large-scale mean *B*-field orientation (29°; Table B1).
[e] $R_{\mathrm{eff}} = \sqrt{ab}$.
[f] Based on the HGBS column density map.
[g] The PA of the outflows is determined based on the midline that passes through the center of the bipolar cones. The outflow data are from Tokuda et al. (2020; see also Ohashi et al. 1997).
[h] The core θ_G is based on the total velocity gradient derived from N_2H^+ data (Punanova et al. 2018). The negative sign corresponds to the angle in the clockwise direction from W to S (see Table B.1 of Punanova et al. 2018).
[i] The core θ_G and PA of the core rotation are perpendicular to each other.

that without this correction factor, the DCF-measured *B*-field strength is overestimated by a factor of 2 when the angular dispersion in the *B*-field is $\leqslant 25°$.

As illustrated in Appendix C, we have used the 850 μm Stokes *I* map to extract core dimensions, column and number densities, and masses. To quantify the nonthermal velocity

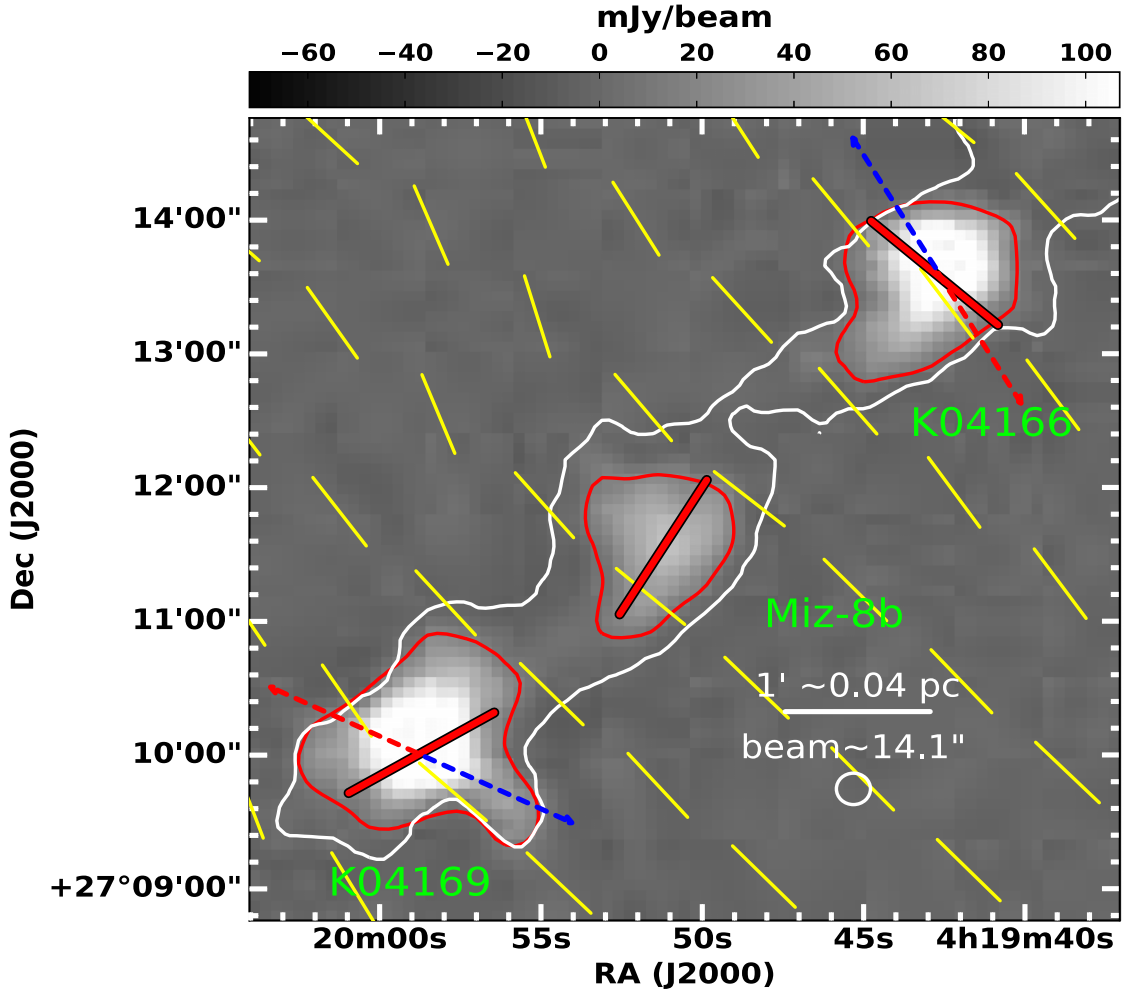

Figure 2. Same as Figure 1(b) but now we only show the mean *B*-field orientation in the three cores K04166, Miz-8b, and K04169, based on the weighted mean of the PAs we measure. The blue and red dashed arrows denote the protostellar outflows (lengths are not to scale) emanating from K04166 and K04169. The red contour around each core is drawn at $I = 13$ mJy beam^{-1}, corresponding to 10σ in total intensity. The large-scale *B*-field morphology, as determined from the oversampled Planck 850 μm polarization data (pixel size 1′), is shown as yellow segments. The white contour is as described in Figure 1(b).

dispersion induced by the turbulence, we estimated the average velocity dispersion ($\delta_{V_{\rm LSR}}$) from archival N_2H^+ (1–0) data (Punanova et al. 2018)[92] obtained using the IRAM 30 m telescope. The spatial and velocity resolutions of the N_2H^+ data are 26.″5 and 0.063 km s^{-1}, respectively. The thermal contributions to the observed velocity dispersions (δ_{V_T}) are estimated (based on the mean dust temperatures of the cores given in Table 2). These components are quadratically subtracted from the observed velocity dispersions ($\delta_{V_{\rm LSR}}$) to obtain nonthermal velocity dispersions ($\delta_{V_{\rm NT}}$). The angular dispersion in the *B*-field is calculated using the relation for the inverse variance–weighted standard deviation of the *B*-field (e.g., Wang et al. 2020). These estimated parameters are listed in Table 2.

Using Equation (1) and the parameters listed above, the *B*-field strength is estimated to be 38 ± 14 μG for K04166, 44 ± 16 μG for K04169, and 12 ± 5 μG for Miz-8b. Since the majority of the *B*-field segments in K04166 and K04169 are confined to the core radii of ∼20″–50″, the *B*-field strengths in these cores are mainly valid to the core envelopes. Further, we caution here that the *B*-field strength of Miz-8b could be highly uncertain because of the limited number of *B*-field segments, and hence the larger angular dispersion, used in the DCF method. The current estimations are similar to the *B*-field strengths of ∼10–100 μG estimated in relatively unperturbed low-mass star-forming regions (Crutcher et al. 2004; Chapman et al. 2011; Crutcher 2012) and 2 orders of magnitude less than the ∼1 mG values estimated in massive star-forming regions (e.g., Curran & Chrysostomou 2007; Hildebrand et al. 2009; Pattle et al. 2017; Liu et al. 2020).

We can use our estimated *B*-field strength to infer the dynamic state and physical properties of the cores (see Table 2). First, we estimate the magnetic and turbulent pressures using the relations $P_B = B^2/8\pi$ and $P_{\rm turb} = \rho\delta^2_{\rm NT}$, respectively. Second, we estimate the Alfvénic Mach number using the relation $M_A = \sqrt{3}\left(\frac{\delta_{\rm NT}}{V_{\rm A}}\right)$, where Alfvén velocity $V_{\rm A} = \frac{B_{\rm los}}{\sqrt{4\pi\,\rho}}$ (where $\rho = n_{\rm H_2}\,\mu\,m_{\rm H}$). Third, we use the mass-to-magnetic flux ratio to infer how important the *B*-field is in comparison to gravity. We measure the mass-to-flux ratio in units of the critical value, as described in Appendix D. Finally, we estimate the rotational energy of each core to determine how rotation may influence the *B*-field in Appendix E. The derived energy values, along with all other parameters, are listed in Table 2.

[92] The data can be found at http://cdsarc.u-strasbg.fr/ftp/J/A+A/617/A27/fits/.

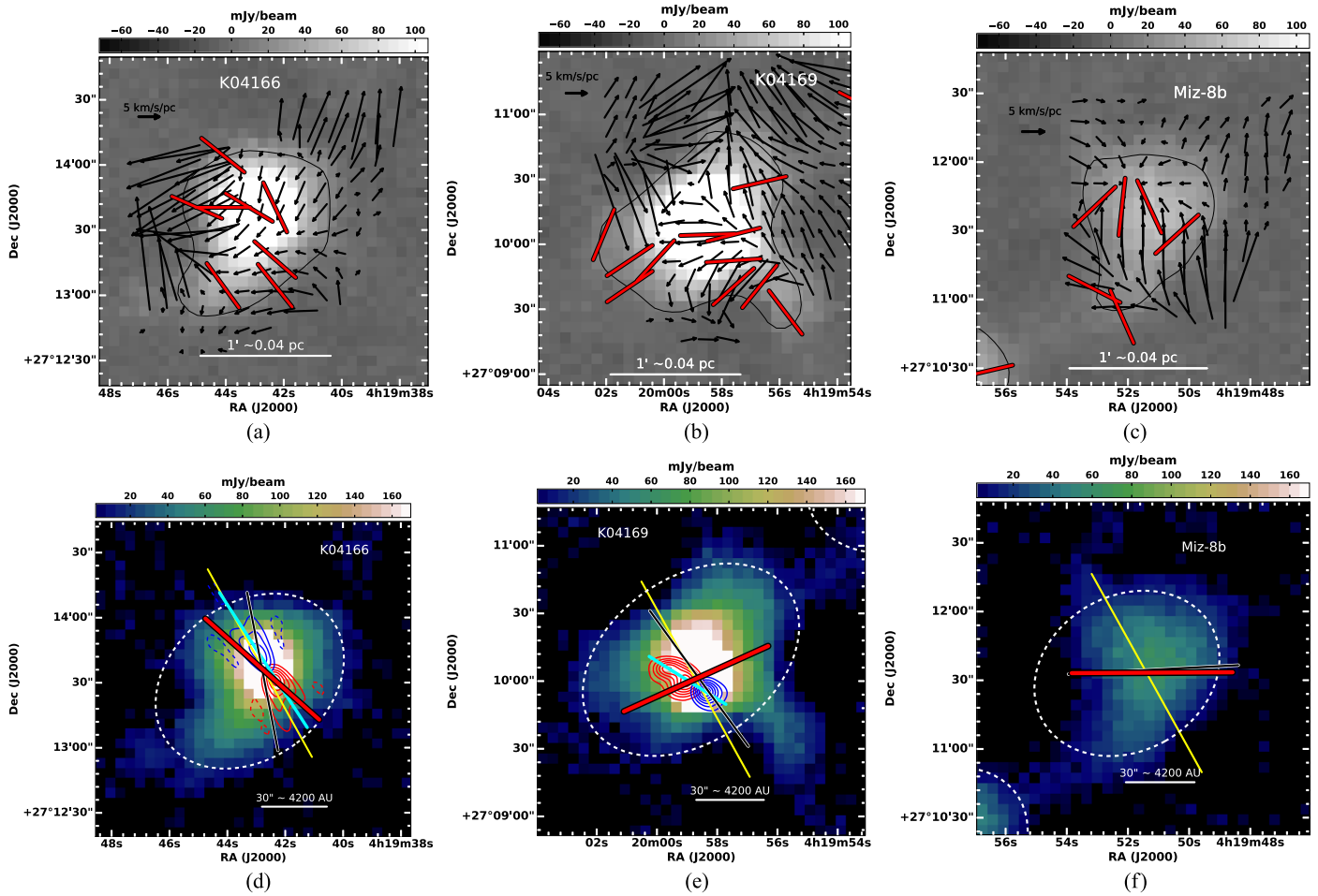

Figure 3. (Top panels) Velocity gradient maps for (a) K04166, (b) K04169, and (c) Miz-8b. The length and angle of each black arrow correspond to the magnitude and direction, respectively, of the local velocity gradient. A reference arrow with units of kilometers per second per parsec is shown on each plot. Red segments show the *B*-field orientations from Figure 1(b). (Bottom panels) Weighted mean *B*-field geometry (thick red segments; same as Figure 2) in the cores of (d) K04166, (e) K04169, and (f) Miz-8b, overlaid on the Stokes *I* map (color scale). The large-scale Planck mean *B*-field direction is shown as a yellow segment on each core. Red and blue contours show the redshifted and blueshifted ^{12}CO (2–1) emission tracing the bipolar outflow in the center of each core. These were obtained with the ALMA 7 m array by Tokuda et al. (2020). The cyan line denotes the mean PA of each outflow (33° for K04166 and 58° for K04169). The thin black line represents the PA of the core rotation axis. The integrated velocity ranges are −10 to 0 and 10 to 20 km s^{-1} for the blue- and redshifted outflows of K04166 and −5 to 4 and 11 to 17 km s^{-1} for the blue- and redshifted outflows of K04169. The lowest and subsequent contour steps are 0.4 and 1.2 K km s^{-1} , respectively. The angular resolution of the ALMA data is $6\farcs8 \times 6\farcs5$.

4. Discussion

Since the two protostellar cores, K04166 and K04169, are at a similar evolutionary stage and share similar characteristics (see Table 2), we discuss their energy parameters and gas kinematics with reference to the differences in *B*-field morphology in Section 4.1. These aspects for the prestellar core Miz-8b are addressed in Section 4.2.

4.1. K04166 and K04169

The magnetic-to-turbulent pressure ratio is seen to be ∼1 in both cores (see Table 2). This suggests that the *B*-field and turbulence are near equilibrium with each other. Equivalently, the Alfvénic Mach number (∼1) suggests that turbulent motions are trans-Alfvénic. Therefore, turbulent motions are not dominant over, and so do not shape the morphology of, the *B*-field in these cores. The mean mass-to-flux ratio criticality of the cores, λ, is found to be ∼1, suggesting that the core envelopes may be magnetically critical and marginally supported by the *B*-field. The ratio of rotational to magnetic energy (see Appendix E) is $E_{\rm rot}/E_{\rm mag} \ll 1$, which infers that the core rotational energy is too weak to alter the *B*-field orientation.

Our analysis indicates that there is an equipartition among magnetic, turbulent, and gravitational energies in the core envelopes of K04166 and K04169. Then the question arises as to why the mean *B*-field orientations in the two cores are different from each other. We use the morphological correspondence between N_2H^+ velocity gradients and the *B*-field, as shown in Figures 3(a) and (b), to shed light on this.

The velocity field in K04166 as inferred from the velocity gradient map is well defined, fairly uniform, and almost perpendicular to the *B*-field segments. This could be interpreted as bulk core rotation, with the angular momentum (or core rotation axis with PA ∼ 11°) being parallel to the *B*-field direction. In addition, the outflow is well collimated and exhibits extremely high velocity components (Wang et al. 2014), suggesting a possible role of the *B*-field in channeling the outflow and transporting energy and angular momentum away from the rotating circumstellar disk. The PAs of the core (and filament) minor axis (∼37°), core rotation axis (∼11°), and bipolar outflows (∼33°) are all roughly aligned with both $\bar{\theta}_{{\rm core},B}$ (48°) and $\theta_B^{\rm largescale}$ (29°) to within ∼30°, as

shown in Figure 3(d). This strong geometrical correspondence suggests that the *B*-field, which is inherited from the large-scale uniform *B*-field, has played a significant role in core evolution by allowing gas contraction along field lines to form the core, subsequently governing its collapse via ambipolar diffusion, and finally collimating the outflows. These signatures are in accordance with the paradigm of the low-mass star formation process driven by ambipolar diffusion in K04166. However, we could not trace an hourglass morphology in the inner core (radii $<20''$ or <2800 au) due to limited resolution ($14\farcs1 \sim 2000$ au).

On the other hand, the velocity gradient map in K04169 appears to be rather complex and displays two converging flows, from the northeast and the southwest (Figure 3(b)). Counterrotation between the disk and the envelope in K04169 is also reported (Takakuwa et al. 2018). We see that the core mean *B*-field ($\bar{\theta}_{\mathrm{core},B} \sim 121°$) is nearly aligned parallel to the mean orientation of the velocity gradient ($\theta_{\mathrm{G}} \sim 126°$; see Table 2). We suggest that this complex gas flow might have altered the *B*-field from being parallel to the core minor axis in the earlier stage to the current perpendicular configuration in K04169. This might have also caused the misalignment of the outflows (PA $\sim 58°$), core rotation axis (PA $\sim 36°$), and core minor axis (PA $\sim 36°$) with $\bar{\theta}_{\mathrm{core},B}$, as shown in Figure 3(e) (see Table 2 for more details).

4.2. Miz-8b

Unlike K04166 and K04169, Miz-8b has a disordered *B*-field. It has a magnetic-to-turbulent pressure ratio of $\sim$0.3 and a Alfvénic Mach number of $\sim$2 (see Table 2), which suggests that turbulence is super-Alfvénic and dominates over the *B*-field. Cores formed in a weakly magnetized, turbulent cloud would have a chaotic *B*-field configuration because of the dominance of turbulent eddies over structural dynamics and field lines (Stone et al. 1998; Ballesteros-Paredes et al. 1999b; Mac Low & Klessen 2004; Li et al. 2014). We suggest that the *B*-fields in Miz-8b are complex because of the dominance of turbulent flows (Figure 3(c)). As a result, the *B*-field is decoupled from the large-scale ordered field (Figure 3(f)). Since the inferred *B*-field strength in Miz-8b is weaker ($12 \pm 5\ \mu$G), it will not support the core against gravity, as the mass-to-flux ratio is found to be supercritical ($\lambda \sim 3$).

5. Summary

We have performed deep dust polarization observations toward the Taurus B213 filament at 850 μm using SCUBA-2 and POL-2 on the JCMT as part of the BISTRO survey. We successfully detected polarized signal in and studied in detail the *B*-field of two protostellar cores (K04166 and K04169) and one prestellar core (Miz-8b) on scales from 2000 au to 0.25 pc. The main findings of this work are as follows.

1. Despite having (i) ordered *B*-fields on large scales and (ii) quiescent physical conditions and (iii) being formed out of the same natal filament, the three B213 cores exhibit diverse magnetic field properties.
2. Among the three cores, only one, K04166, retains a memory of the large-scale *B*-field, with a field orientation consistent with those seen on larger scales. The other two cores appear to have decoupled from the large-scale field.
3. Using the DCF method, we estimate the *B*-field strengths in K04166, K04169, and Miz-8b to be 38 ± 14, 44 ± 16, and $12 \pm 5\ \mu$G, respectively. The associated magnetic energies are in equipartition with both turbulent and gravitational energies in the core envelopes of K04166 and K04169 while being much smaller than the turbulent energy in the core of Miz-8b.
4. Based on the correlation between the PAs of the core-scale *B*-field, the large-scale field, the minor axis of the core, outflows, and the core rotation axis, we suggest that the formation and evolution of K04166 are regulated by the *B*-field, consistent with the paradigm of low-mass star formation via ambipolar diffusion. However, as revealed by their complex velocity fields, the evolution of the other two cores, K04169 and Miz-8b, could be regulated by converging accretion flows and turbulent motions, respectively.

We suggest that cores formed in a magnetically regulated molecular cloud may not necessarily retain a memory of the large-scale *B*-field of the cloud in which they form. Instead, localized differences in gas kinematics, which probably arise due to gas inflows onto the filament, can affect the role of the *B*-field in the star formation process and the subsequent properties of the forming systems.

We thank the referee for constructive suggestions that have improved the content and flow of this paper. This work is supported by National Natural Science Foundation of China (NSFC) grant Nos. 11988101, 11725313, and U1931117 and the International Partnership Program of Chinese Academy of Sciences grant No. 114A11KYSB20160008. This work is also supported by Special Funding for Advanced Users, budgeted and administrated by the Center for Astronomical Mega-Science, Chinese Academy of Sciences (CAMS). C.E. thanks Tokuda Kazuki for kindly providing us with the ALMA data on the protostellar outflows. C.E. thanks Sihan Jiao and Yuehui Ma for help with the analyses. K.Q. acknowledges support from the National Natural Science Foundation of China (NSFC) through grant U1731237. C.W.L. is supported by the Basic Science Research Program through the National Research Foundation of Korea (NRF) funded by the Ministry of Education, Science and Technology (NRF-2019R1A2C1010851). N.O. is supported by Ministry of Science and Technology (MOST) grant MOST 109-2112-M-001-051 in Taiwan. C.L.H.H. acknowledges the support of the NAOJ Fellowship and JSPS KAKENHI grants 18K13586 and 20K14527. W.K. was supported by the New Faculty Startup Fund from Seoul National University. D.J. is supported by the National Research Council of Canada and a Natural Sciences and Engineering Research Council of Canada (NSERC) Discovery Grant. A.S. acknowledges support from the NSF through grant AST-1715876. K.H.K is supported by the center for Women In Science, Engineering and Technology (WISET) grant funded by the Ministry of Science and ICT (MSIT) under the program for returners into R&D (WISET-2019-288; WISET-2020-247). P.N. D and N.B.N are funded by Vietnam National Foundation for Science and Technology Development (NAFOSTED) under grant number 103.99-2019.368. Y.W.T acknowledges the grant MOST 108-2112-M-001-004-MY2.

The James Clerk Maxwell Telescope is operated by the East Asian Observatory on behalf of the National Astronomical Observatory of Japan, the Academia Sinica Institute of Astronomy and Astrophysics, the Korea Astronomy and Space Science Institute, and the Center for Astronomical Mega-Science. Additional funding support is provided by the Science and Technology Facilities Council of the United Kingdom and participating universities in the United Kingdom, Canada, and Ireland.

Facility: JCMT.

Appendix A
Polarization Properties: Detection of Weakly Polarized Dust Emission

Figure A1 plots PI versus I for each core, using the selection criterion $I/\sigma_I > 10$ (gray filled circles). In at least three cores, K04166, Miz-8b, and K04169, and also in the plot showing all of the cores, a slowly increasing trend in PI can be seen up to $I \sim 100$ mJy beam^{-1}, beyond which PI remains approximately constant, although there exist fewer data points.

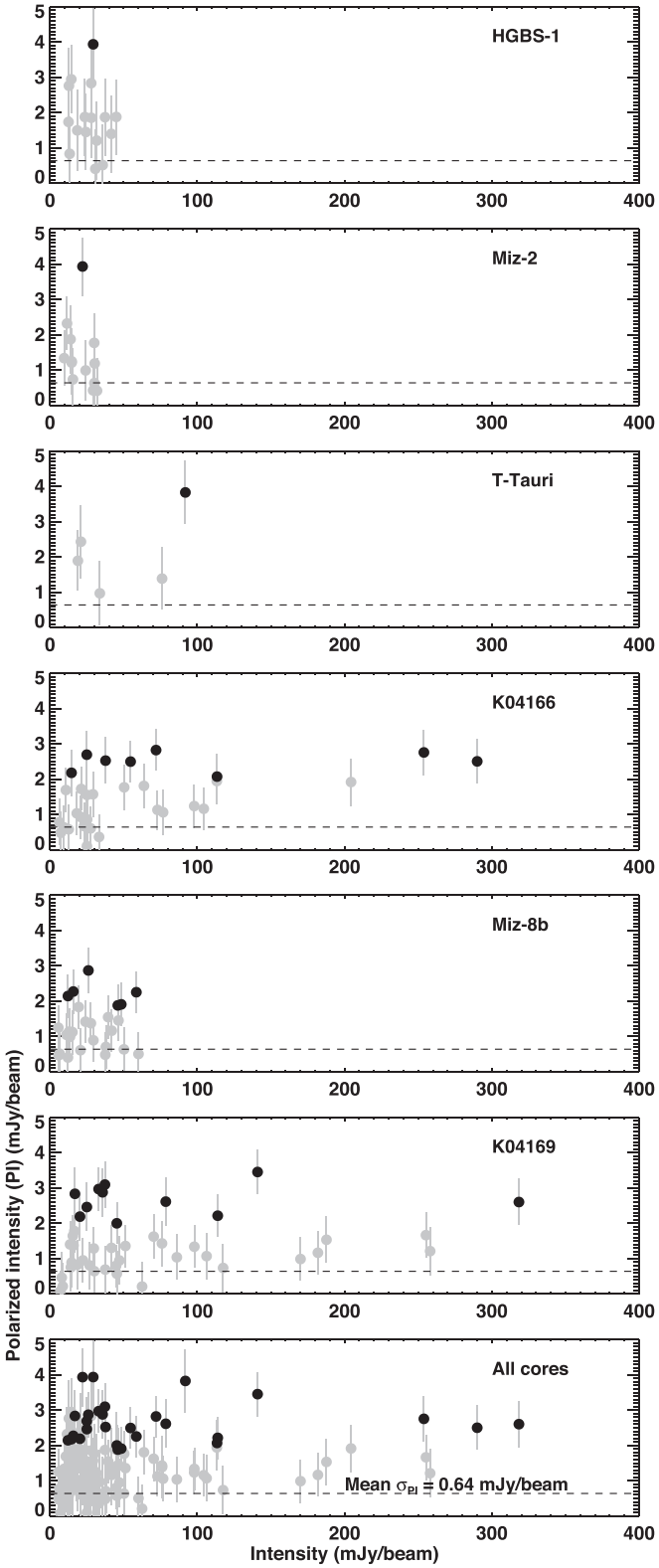

Figure A1. The PI vs. intensity (I) plots for each core and all of the cores combined. The name of the core is stated in each panel. Gray filled circles represent the data satisfying the criterion $I/\sigma_I > 10$, whereas black filled circles denote those satisfying both criteria, $I/\sigma_I > 10$ and $P/\sigma_P \geqslant 3$. The dashed line represents the median $\sigma_{\rm PI} = 0.64$ mJy beam^{-1} determined from the black filled circles.

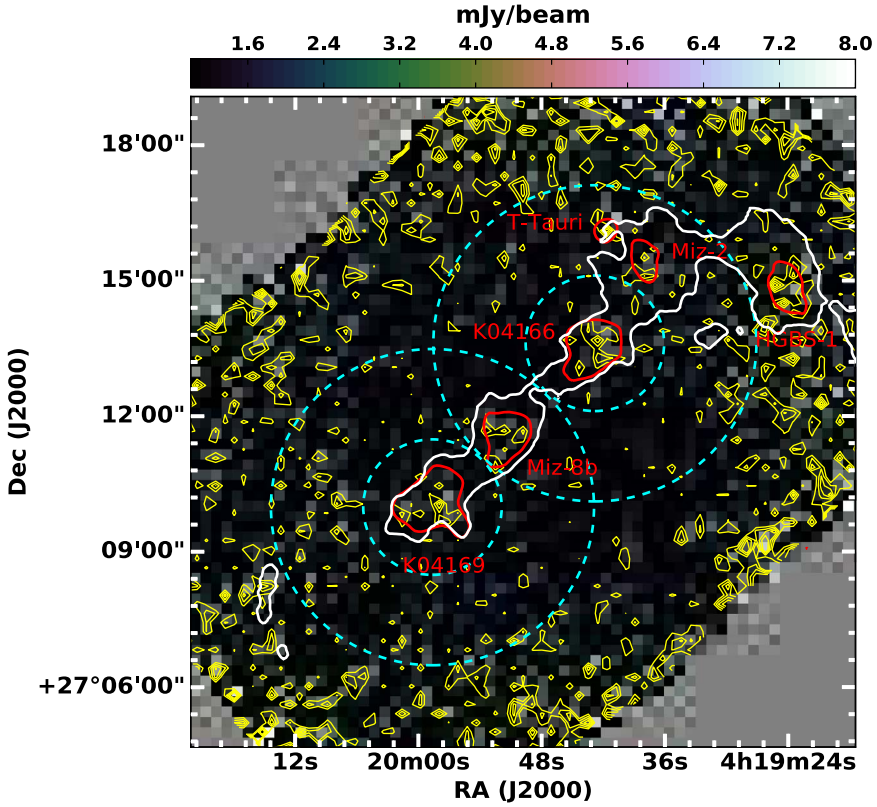

Figure A2. Debiased PI map produced using our POL-2 Stokes Q and U maps of the B213 region. Nonsmoothed PI contours are drawn at [2, 3, 4] $\times$ $\sigma_{\rm PI}$, where $\sigma_{\rm PI}$ is the rms noise, $\sim$1 mJy beam^{-1} (estimated using the pixels in a signal-free region of the PI map). The red contour corresponds to a POL-2 total intensity of 13 mJy beam^{-1}. The PI is nearly zero in the area surrounding the cores, but within the cores themselves, a clear detection can be seen. Cyan dashed circles mark the areas with diameters of 3′ and 7′ around the central positions of the two observed fields. Polarization measurements within the smaller circles, as well as the common area covered by both larger circles, should be useful. Therefore, the measurements of the three cores T Tauri, Miz-2, and HGBS-1 may not be reliable due to the dominance of background noise at their locations. Each of the six cores are labeled.

To extract the reliable data from our POL-2 measurements of the B213 cores, we adopt the selection criteria $I/\sigma_I > 10$ and $P/\sigma_P > 3$, which yield 28 polarization measurements (black filled circles in Figure A1). The resulting median $\sigma_{\rm PI}$ is 0.64 mJy beam^{-1}. The PI values lie in the range 1.88–3.94 mJy beam^{-1}, with a median of 2.60 mJy beam^{-1}, whereas I ranges from 13 to 318 mJy beam^{-1}, as shown in Figure A1. The P values lie in the range 0.82%–17.8% with a minimum of $\sim$1%, median of $\sim$7%, and standard deviation of $\sim$5%. Above the 3σ level in PI, a clear detection of PI (yellow contours) within the core boundaries determined from the Stokes I map (red contour at 13 mJy beam^{-1}) can be seen in the PI map, as shown in Figure A2.

Appendix B
B-field at Larger Scales ($\sim$0.2–2.4 pc) Determined from Optical, NIR, and Planck Polarization Data

In order to compare the core-scale B-field (see Section 3.1) with that in the large-scale, low-density surrounding region,

Table B1
Mean *B*-field Orientations, Determined from Optical, NIR, and Low-resolution Submillimeter (Planck/850 μm) Polarization Observations

Wavelength (1)	Diameter (arcmin) (2)	No. of Stars/Segments (3)	$\theta_B^{\rm largescale} \pm \sigma$ (deg) (4)	Offset PA (deg) (5)
Optical[a]	60	15	29 ± 14	104
NIR	60	42	37 ± 17	96
Submillimeter (Planck[b])	60	445	29 ± 17	104

Notes. Here $\theta_B^{\rm largescale} \pm \sigma$ are the mean and standard deviation values resulting from a Gaussian distribution fitted to the data. Offset PA is the difference in angle between the PA of the B213 filament ($\sim$133°) and the large-scale mean *B*-field ($\theta_B^{\rm largescale}$; column (5)).
[a] Two measurements with significant deviation in either *P* or θ are excluded from the optical data.
[b] Pixels with values <0.008 $K_{\rm CMB}$ have been excluded from the Planck data in order to prevent randomization of our inferred *B*-field direction by measurements dominated by noise.

we make use of archival optical, NIR, and Planck/850 μm low-resolution dust polarization data,[93] and the *B*-field morphologies inferred from these data sets are shown in Figure 1. We select the data within 1° of B213; the resulting values of the Gaussian mean and standard deviation in *B*-field orientation ($\theta_B^{\rm largescale} \pm \sigma$) are given in Table B1. There exist a significant number of optical/NIR *B*-field segments around B213; however, NIR polarization measurements are confined to an area to the west of B213 and therefore may not reveal the local *B*-field of B213. Visual inspection suggests that an optical- and Planck-inferred *B*-field is ordered. This is confirmed by their mean *B*-field orientations, which are respectively found to be $29° \pm 14°$ and $29° \pm 17°$. These values are nearly identical, with slightly different standard deviations (see Table B1), whereas NIR polarization data show a curved morphology, which follows the compressed and curved shell of LDN 1495 with a slightly different mean *B*-field orientation of $37° \pm 17°$. Therefore, to delineate the mean *B*-field in and around B213, we select the optical and Planck polarization data within 1° of B213, which yielded a mean orientation of 29°. This large-scale, coherent *B*-field ($\theta_B^{\rm largescale}$) with a mean orientation of 29° spans spatial scales from $\sim$0.2 pc ($\sim 5'$ resolution of Planck) to $\sim$2.4 pc (1° area around B213).

Appendix C
Geometries, Effective Radii, Masses, and Column and Number Densities of B213 Cores

To estimate various energy and pressure terms for the cores, we extract their masses and column and number densities from the POL-2 Stokes *I* map. For this, core dimensions are obtained by fitting the ellipse function *mpfitellipse.pro* from the Marquardt library to the 10σ Stokes *I* contours (13 mJy beam^{-1}) of each core. The resulting core dimensions (a = semimajor and b = semiminor), effective radius ($R_{\rm eff} = \sqrt{ab}$), and PA in degrees east of north are given in Table 2.

The integrated fluxes (F_ν) and median dust temperatures ($T_{\rm d}$; from the Herschel Gould Belt Survey (HGBS) temperature map) over the core are used to estimate core masses using the relation (Hildebrand 1983)

$$M = \frac{F_\nu\, D^2}{B_\nu(T_{\rm d})\,\kappa_\nu}, \tag{C1}$$

where $D = 140$ pc is the distance of B213, $\kappa_\nu = 0.0125$ cm^2 g^{-1} (e.g., Johnstone et al. 2017) is the dust mass opacity, and $B_\nu(T_{\rm d})$ is the Planck function for a blackbody at temperature $T_{\rm d}$. The uncertainty in mass is estimated by propagating the standard deviation in $T_{\rm d}$, 10% of the value of F_ν as the flux calibration uncertainty of SCUBA-2 (Dempsey et al. 2013), and a 50% uncertainty in dust mass opacity (e.g., Roy et al. 2014).

The column and number densities of the cores are estimated using the following relations:

$$N({\rm H_2}) = \frac{M}{\mu\, m_{\rm H}\, \pi\, R_{\rm eff}^2} \tag{C2}$$

and

$$n({\rm H_2}) = \frac{3\, M}{4\, \mu\, m_{\rm H}\, \pi\, R_{\rm eff}^3}. \tag{C3}$$

Estimated masses and column and number densities and their corresponding uncertainties are given along with $T_{\rm d}$ and F_ν values in Table 2.

Appendix D
Mass-to-flux Ratio Criticality

To infer the importance of the *B*-field with respect to the gravity, we estimate the mass-to-magnetic flux ratio in units of the critical value (hereafter mass-to-flux ratio criticality) using the following relation (Crutcher et al. 2004; Chapman et al. 2011),

$$\lambda = \frac{(M/\phi)}{(M/\phi)_{\rm crit}} = 7.6\, N_{\|}({\rm H_2})\,/B_{\rm tot}, \tag{D1}$$

where $N_{\|}({\rm H_2})$ is the mean column density ($N({\rm H_2})_{\rm POL2}$) in units of 10^{21} cm^{-2} along the magnetic flux tube, and $B_{\rm tot}$ is the total *B*-field strength in μG. The critical mass-to-flux ratio, $(M/\phi)_{\rm crit} = 1/\sqrt{(4\pi^2 G)}$ (Nakano & Nakamura 1978), corresponds to the stability criterion for an isothermal gaseous layer threaded by a perpendicular *B*-field. A cloud region with $(M/\phi) > (M/\phi_{\rm crit})$, i.e., $\lambda > 1$, will collapse under its own gravity, so such a cloud is considered to be supercritical. A cloud with $\mu < 1$ will be in a subcritical state because of the significant support rendered by the

[93] Planck 353 GHz (850 μm) dust continuum polarization data, comprising Stokes *I*, *Q*, and *U* maps for the B213 region, have been extracted from the Planck Public Data Release 2 of Multiple Frequency Cutout Visualization (PR2 Full Mission Map with PCCS2 Catalog: https://irsa.ipac.caltech.edu/applications/planck/). The data have been reduced using the standard procedures described by Planck Collaboration et al. (2015, 2016b), Soler et al. (2016), Baug et al. (2020), and references therein.

B-field. Taking the mean $N(H_2)=N_{\|}(H_2)$ as $(10\pm6)\times10^{21}$, $(11\pm6)\times10^{21}$, and $(5\pm3)\times10^{21}$ cm^{-2} and $B=B_{\rm tot}$ as 38 ± 17, 48 ± 22, and 12 ± 5 μG, we estimate μ values of 2 ± 1, 2 ± 1, and 3 ± 2 for K04166, K04169, and Miz-8b, respectively.

However, considering (i) the projection effects between $N_{\|}(H_2)/B_{\rm tot}$ and the actual measured $N(H_2)/B_{\|}$ (where $B_{\|}$ is the plane-of-the-sky B-field strength), (ii) the B-field being perpendicular to the core elongation in the case of an oblate spheroid or parallel to the core elongation in the case of a prolate spheroid, and (iii) the assumption that the B-field is randomly oriented with respect to the line of sight, the actual value of μ becomes $(1/3)\lambda_{\rm obs}$ for K04166, as the mean B-field is perpendicular to the core major axis, and $(3/4)\lambda_{\rm obs}$ for K04169, as the mean B-field is parallel to the major axis (Planck Collaboration et al. 2016a; see their Appendix D.4[94]). No correction was applied on the λ value of Miz-8b because of the misalignment between the mean B-field and core major axis. Therefore, the resulting λ values are 0.7 ± 0.5, 1.4 ± 1.0, and 3 ± 1, which are given in Table 2.

Appendix E
Ratio of Magnetic-to-rotational Energy

By assuming that the cores are uniform density spheres, we measure the rotational and magnetic energies using the following relations (see Wurster & Lewis 2020):

$$E_{\rm rot}=\frac{pMR^2\Omega^2}{5} \tag{E1}$$

and

$$E_{\rm mag}=\frac{B^2V}{8\pi}. \tag{E2}$$

In Equation (E1), the correction factor, $p=\frac{2(3-\mathcal{A})}{3(5-\mathcal{A})}=0.27$ (where $\mathcal{A}$ is the power index in the density distribution of the form $\rho\propto r^{-\mathcal{A}}$ and we consider $\mathcal{A}=1.6$), accounts for the density distribution in the sphere (see Xu et al. 2020 for more details). We use the effective radii $R=R_{\rm eff}=\sqrt{ab}$ (where $a=$ semimajor axis and $b=$ semiminor axis), and the volume of the core $V=(4/3)\pi R_{\rm eff}^3$. Here Ω is the angular velocity or magnitude of the velocity gradient of the core measured from the N_2H^+ data and is found to be 2.05 ± 0.02 km s^{-1} pc^{-1} for K04166, 3.86 ± 0.04 km s^{-1} pc^{-1} for K04169, and 1.88 ± 0.02 km s^{-1} pc^{-1} for Miz-8b (Punanova et al. 2018; see their Table B.2). Here M is the mass of the cores (see Appendix C). The derived energy values and their ratios are given in Table 2.

Appendix F
Morphological Correlation between the B-field and the Gradients of Velocity

We model the observed line-of-sight centroid velocities of N_2H^+ ($V_{\rm LSR}$, km s^{-1}) and the corresponding offset length scales in sky coordinates (R.A (Δ_α in pc) and decl. (Δ_δ in pc)) around each pixel in terms of velocity gradients in R.A (∇_{V_α}, km s^{-1} pc^{-1}) and decl. (∇_{V_δ}, km s^{-1} pc^{-1}) and the constant systematic velocity of that reference pixel (V_0, km s^{-1}) using a first-degree bivariate polynomial of the form (Goodman et al. 1993; Henshaw et al. 2016; Sokolov et al. 2018)

$$V_{\rm LSR}=V_0+\nabla_{V_\alpha}\Delta_\alpha+\nabla_{V_\delta}\Delta_\delta. \tag{F1}$$

We have used the IDL algorithm *mpfit* to perform weighted, nonlinear, minimum χ^2 fitting to constrain the velocity gradients ∇_{V_α} and ∇_{V_δ} and their corresponding uncertainties. These are further used to derive the magnitude ($\mathcal{G}$) and direction ($\Theta_{\mathcal{G}}$) of the velocity gradients using the following relations:

$$\mathcal{G}\equiv|\nabla_V|=\sqrt{\nabla_{V_\alpha}^2+\nabla_{V_\delta}^2} \tag{F2}$$

and

$$\Theta_{\mathcal{G}}=\arctan\left(\frac{\nabla_{V_\alpha}}{\nabla_{V_\delta}}\right). \tag{F3}$$

We considered at least six adjacent pixels lying within the beam size of the IRAM 30 m telescope for N_2H^+ (1–0), 26.″5, around each pixel when the fitting was performed. In addition, we estimated the uncertainties in the velocity gradients using Equation (2) of Punanova et al. (2018). These were used as weights while performing the weighted fits. The top panels of Figure 3 show velocity gradients superimposed on the POL-2 Stokes I maps of K04166, K04169, and Miz-8b.

[94] In order to correct the estimated mass-to-flux ratio (in critical units) for projection effects, a factor of 1/2 is valid for a spheroid cloud, 1/3 for an oblate spheroid flattened perpendicular to the B-field, and 3/4 for a prolate spheroid elongated along the B-field.

ORCID iDs

Chakali Eswaraiah https://orcid.org/0000-0003-4761-6139
Ray S. Furuya https://orcid.org/0000-0003-0646-8782
Tetsuo Hasegawa https://orcid.org/0000-0003-1853-0184
Derek Ward-Thompson https://orcid.org/0000-0003-1140-2761
Keping Qiu https://orcid.org/0000-0002-5093-5088
Nagayoshi Ohashi https://orcid.org/0000-0003-0998-5064
Kate Pattle https://orcid.org/0000-0002-8557-3582
Sarah Sadavoy https://orcid.org/0000-0001-7474-6874
Charles L. H. Hull https://orcid.org/0000-0002-8975-7573
David Berry https://orcid.org/0000-0001-6524-2447
Yasuo Doi https://orcid.org/0000-0001-8746-6548
Tao-Chung Ching https://orcid.org/0000-0001-8516-2532
Shih-Ping Lai https://orcid.org/0000-0001-5522-486X
Jia-Wei Wang https://orcid.org/0000-0002-6668-974X
Patrick M. Koch https://orcid.org/0000-0003-2777-5861
Jungmi Kwon https://orcid.org/0000-0003-2815-7774
Woojin Kwon https://orcid.org/0000-0003-4022-4132
Pierre Bastien https://orcid.org/0000-0002-0794-3859
Doris Arzoumanian https://orcid.org/0000-0002-1959-7201
Simon Coudé https://orcid.org/0000-0002-0859-0805
Archana Soam https://orcid.org/0000-0002-6386-2906
Lapo Fanciullo https://orcid.org/0000-0001-9930-9240
Hsi-Wei Yen https://orcid.org/0000-0003-1412-893X
Junhao Liu https://orcid.org/0000-0002-4774-2998
Thiem Hoang https://orcid.org/0000-0003-2017-0982
Wen Ping Chen https://orcid.org/0000-0003-0262-272X
Yoshito Shimajiri https://orcid.org/0000-0001-9368-3143
Tie Liu https://orcid.org/0000-0002-5286-2564
Zhiwei Chen https://orcid.org/0000-0003-0849-0692
Hua-bai Li https://orcid.org/0000-0003-2641-9240
A-Ran Lyo https://orcid.org/0000-0002-9907-8427
Jihye Hwang https://orcid.org/0000-0001-7866-2686
Doug Johnstone https://orcid.org/0000-0002-6773-459X

Ramprasad Rao https://orcid.org/0000-0002-1407-7944
Nguyen Bich Ngoc https://orcid.org/0000-0002-5913-5554
Pham Ngoc Diep https://orcid.org/0000-0002-2808-0888
Steve Mairs https://orcid.org/0000-0002-6956-0730
Harriet Parsons https://orcid.org/0000-0002-6327-3423
Motohide Tamura https://orcid.org/0000-0002-6510-0681
Mehrnoosh Tahani https://orcid.org/0000-0001-8749-1436
Huei-Ru Vivien Chen https://orcid.org/0000-0002-9774-1846
Fumitaka Nakamura https://orcid.org/0000-0001-5431-2294
Hiroko Shinnaga https://orcid.org/0000-0001-9407-6775
Ya-Wen Tang https://orcid.org/0000-0002-0675-276X
Jungyeon Cho https://orcid.org/0000-0003-1725-4376
Chang Won Lee https://orcid.org/0000-0002-3179-6334
Shu-ichiro Inutsuka https://orcid.org/0000-0003-4366-6518
Kazunari Iwasaki https://orcid.org/0000-0002-2707-7548
Lei Qian https://orcid.org/0000-0003-0597-0957
Jinjin Xie https://orcid.org/0000-0002-2738-146X
Hong-Li Liu https://orcid.org/0000-0003-3343-9645
Chuan-Peng Zhang https://orcid.org/0000-0002-4428-3183
Jianjun Zhou https://orcid.org/0000-0003-0356-818X
Philippe André https://orcid.org/0000-0002-3413-2293
Sheng-Yuan Liu https://orcid.org/0000-0003-4603-7119
Xing Lu https://orcid.org/0000-0003-2619-9305
Tyler L. Bourke https://orcid.org/0000-0001-7491-0048
Do-Young Byun https://orcid.org/0000-0003-1157-4109
David Eden https://orcid.org/0000-0002-5881-3229
Brenda Matthews https://orcid.org/0000-0003-3017-9577
Laura M. Fissel https://orcid.org/0000-0002-4666-609X
Kee-Tae Kim https://orcid.org/0000-0003-2412-7092
Chin-Fei Lee https://orcid.org/0000-0002-3024-5864
Jongsoo Kim https://orcid.org/0000-0002-1229-0426
Tae-Soo Pyo https://orcid.org/0000-0002-3273-0804
Antonio Chrysostomou https://orcid.org/0000-0002-9583-8644
Eun Jung Chung https://orcid.org/0000-0003-0014-1527
Le Ngoc Tram https://orcid.org/0000-0002-6488-8227
Erica Franzmann https://orcid.org/0000-0003-2142-0357
Per Friberg https://orcid.org/0000-0002-8010-8454
Rachel Friesen https://orcid.org/0000-0001-7594-8128
Gary Fuller https://orcid.org/0000-0001-8509-1818
Tim Gledhill https://orcid.org/0000-0002-2859-4600
Sarah Graves https://orcid.org/0000-0001-9361-5781
Matt Griffin https://orcid.org/0000-0002-0033-177X
Qilao Gu https://orcid.org/0000-0002-2826-1902
Jennifer Hatchell https://orcid.org/0000-0002-4870-2760
Martin Houde https://orcid.org/0000-0003-4420-8674
Koji Kawabata https://orcid.org/0000-0001-6099-9539
Il-Gyo Jeong https://orcid.org/0000-0002-5492-6832
Ji-hyun Kang https://orcid.org/0000-0001-7379-6263
Sung-ju Kang https://orcid.org/0000-0002-5004-7216
Miju Kang https://orcid.org/0000-0002-5016-050X
Akimasa Kataoka https://orcid.org/0000-0003-4562-4119
Francisca Kemper https://orcid.org/0000-0003-2743-8240
Mark Rawlings https://orcid.org/0000-0002-6529-202X
Jonathan Rawlings https://orcid.org/0000-0001-5560-1303
John Richer https://orcid.org/0000-0002-9693-6860
Andrew Rigby https://orcid.org/0000-0002-3351-2200
Giorgio Savini https://orcid.org/0000-0003-4449-9416
Anna Scaife https://orcid.org/0000-0002-5364-2301
Gwanjeong Kim https://orcid.org/0000-0003-2011-8172
Kyoung Hee Kim https://orcid.org/0000-0001-9597-7196
Mi-Ryang Kim https://orcid.org/0000-0002-1408-7747
Florian Kirchschlager https://orcid.org/0000-0002-3036-0184
Jason Kirk https://orcid.org/0000-0002-4552-7477
Masato I. N. Kobayashi https://orcid.org/0000-0003-3990-1204
Vera Konyves https://orcid.org/0000-0002-3746-1498
Takayoshi Kusune https://orcid.org/0000-0002-9218-9319
Kevin Lacaille https://orcid.org/0000-0001-9870-5663
Chi-Yan Law https://orcid.org/0000-0003-1964-970X
Sang-Sung Lee https://orcid.org/0000-0002-6269-594X
Yong-Hee Lee https://orcid.org/0000-0001-6047-701X
Masafumi Matsumura https://orcid.org/0000-0002-6906-0103
Gerald Moriarty-Schieven https://orcid.org/0000-0002-0393-7822
Tetsuya Nagata https://orcid.org/0000-0001-9264-9015
Takashi Onaka https://orcid.org/0000-0002-8234-6747
Geumsook Park https://orcid.org/0000-0001-8467-3736
Xindi Tang https://orcid.org/0000-0002-4154-4309
Kohji Tomisaka https://orcid.org/0000-0003-2726-0892
Serena Viti https://orcid.org/0000-0001-8504-8844
Hongchi Wang https://orcid.org/0000-0003-0746-7968
Hyunju Yoo https://orcid.org/0000-0002-8578-1728
Yapeng Zhang https://orcid.org/0000-0002-5102-2096
Sam Falle https://orcid.org/0000-0002-9829-0426
Jean-François Robitaille https://orcid.org/0000-0001-5079-8573

References

Allen, A., Li, Z.-Y., & Shu, F. H. 2003, ApJ, 599, 363
Alves, F. O., Franco, G. A. P., & Girart, J. M. 2008, A&A, 486, L13
André, P., Di Francesco, J., Ward-Thompson, D., et al. 2014, in Protostars and Planets VI, ed. H. Beuther et al. (Tucson, AZ: Univ. Arizona Press), 27
Arthur, S. J., Henney, W. J., Mellema, G., de Colle, F., & Vázquez-Semadeni, E. 2011, MNRAS, 414, 1747
Ballesteros-Paredes, J., Hartmann, L., & Vázquez-Semadeni, E. 1999a, ApJ, 527, 285
Ballesteros-Paredes, J., Vázquez-Semadeni, E., & Scalo, J. 1999b, ApJ, 515, 286
Baug, T., Wang, K., Liu, T., et al. 2020, ApJ, 890, 44
Berry, D. S., Gledhill, T. M., Greaves, J. S., & Jenness, T. 2005, in ASP Conf. Ser. 343, Astronomical Polarimetry: Current Status and Future Directions, ed. A. Adamson et al. (San Francisco, CA: ASP), 71
Bracco, A., Palmeirim, P., André, P., et al. 2017, A&A, 604, A52
Chandrasekhar, S., & Fermi, E. 1953, ApJ, 118, 113
Chapin, E. L., Berry, D. S., Gibb, A. G., et al. 2013, MNRAS, 430, 2545
Chapman, N. L., Goldsmith, P. F., Pineda, J. L., et al. 2011, ApJ, 741, 21
Ching, T.-C., Lai, S.-P., Zhang, Q., et al. 2017, ApJ, 838, 121
Ching, T.-C., Lai, S.-P., Zhang, Q., et al. 2018, ApJ, 865, 110
Coudé, S., Bastien, P., Houde, M., et al. 2019, ApJ, 877, 88
Crutcher, R. M. 2012, ARA&A, 50, 29
Crutcher, R. M., Nutter, D. J., Ward-Thompson, D., & Kirk, J. M. 2004, ApJ, 600, 279
Curran, R. L., & Chrysostomou, A. 2007, MNRAS, 382, 699
Davidson, J. A., Novak, G., Matthews, T. G., et al. 2011, ApJ, 732, 97
Davis, C. J., Chrysostomou, A., Hatchell, J., et al. 2010, MNRAS, 405, 759
Davis, L. 1951, PhRv, 81, 890
Dempsey, J. T., Friberg, P., Jenness, T., et al. 2013, MNRAS, 430, 2534
Doi, Y., Hasegawa, T., Furuya, R. S., et al. 2020, ApJ, 899, 28
Elias, J. H. 1978, ApJ, 224, 857
Eswaraiah, C., Li, D., Samal, M. R., et al. 2020, ApJ, 897, 90
Fiedler, R. A., & Mouschovias, T. C. 1992, ApJ, 391, 199
Fiedler, R. A., & Mouschovias, T. C. 1993, ApJ, 415, 680
Friberg, P., Bastien, P., Berry, D., et al. 2016, Proc. SPIE, 9914, 991403
Friberg, P., Berry, D., Savini, G., et al. 2018, Proc. SPIE, 10708, 107083M
Galli, D., & Shu, F. H. 1993, ApJ, 417, 220
Girart, J. M., Rao, R., & Marrone, D. P. 2006, Sci, 313, 812
Goodman, A. A., Bastien, P., Myers, P. C., & Menard, F. 1990, ApJ, 359, 363
Goodman, A. A., Benson, P. J., Fuller, G. A., & Myers, P. C. 1993, ApJ, 406, 528
Goodman, A. A., Jones, T. J., Lada, E. A., & Myers, P. C. 1992, ApJ, 399, 108
Hartmann, L. 2002, ApJ, 578, 914

Hartmann, L., Ballesteros-Paredes, J., & Bergin, E. A. 2001, ApJ, 562, 852
Heiles, C. 2000, AJ, 119, 923
Henshaw, J. D., Longmore, S. N., Kruijssen, J. M. D., et al. 2016, MNRAS, 457, 2675
Heyer, M. H., Vrba, F. J., Snell, R. L., et al. 1987, ApJ, 321, 855
Hildebrand, R. H. 1983, QJRAS, 24, 267
Hildebrand, R. H., Kirby, L., Dotson, J. L., Houde, M., & Vaillancourt, J. E. 2009, ApJ, 696, 567
Holland, W. S., Bintley, D., Chapin, E. L., et al. 2013, MNRAS, 430, 2513
Hull, C. L. H., Girart, J. M., Tychoniec, Ł., et al. 2017a, ApJ, 847, 92
Hull, C. L. H., Mocz, P., Burkhart, B., et al. 2017b, ApJL, 842, L9
Hull, C. L. H., Plambeck, R. L., Bolatto, A. D., et al. 2013, ApJ, 768, 159
Hull, C. L. H., Plambeck, R. L., Kwon, W., et al. 2014, ApJS, 213, 13
Hull, C. L. H., & Zhang, Q. 2019, FrASS, 6, 3
Johnstone, D., Ciccone, S., Kirk, H., et al. 2017, ApJ, 836, 132
Kenyon, S. J., Calvet, N., & Hartmann, L. 1993, ApJ, 414, 676
Kenyon, S. J., Hartmann, L. W., Strom, K. M., & Strom, S. E. 1990, AJ, 99, 869
Kwon, J., Doi, Y., Tamura, M., et al. 2018, ApJ, 859, 4
Li, H., Griffin, G. S., Krejny, M., et al. 2006, ApJ, 648, 340
Li, H.-b., Dowell, C. D., Goodman, A., Hildebrand, R., & Novak, G. 2009, ApJ, 704, 891
Li, Z.-Y., Krasnopolsky, R., Shang, H., & Zhao, B. 2014, ApJ, 793, 130
Liu, J., Qiu, K., Berry, D., et al. 2019, ApJ, 877, 43
Liu, J., Zhang, Q., Qiu, K., et al. 2020, ApJ, 895, 142
Mac Low, M.-M., & Klessen, R. S. 2004, RvMP, 76, 125
Marsh, K. A., Kirk, J. M., André, P., et al. 2016, MNRAS, 459, 342
McKee, C. F., & Ostriker, E. C. 2007, ARA&A, 45, 565
Mestel, L., & Spitzer, L. J. 1956, MNRAS, 116, 503
Mizuno, A., Onishi, T., Hayashi, M., et al. 1994, Natur, 368, 719
Mocz, P., Burkhart, B., Hernquist, L., McKee, C. F., & Springel, V. 2017, ApJ, 838, 40
Mouschovias, T. C. 1991, ApJ, 373, 169
Mouschovias, T. C., & Spitzer, L. J. 1976, ApJ, 210, 326
Mouschovias, T. C., Tassis, K., & Kunz, M. W. 2006, ApJ, 646, 1043
Nakano, T., & Nakamura, T. 1978, PASJ, 30, 671
Ohashi, N., Hayashi, M., Ho, P. T. P., et al. 1997, ApJ, 488, 317
Ostriker, E. C., Stone, J. M., & Gammie, C. F. 2001, ApJ, 546, 980
Palmeirim, P., André, P., Kirk, J., et al. 2013, A&A, 550, A38
Pattle, K., Lai, S.-P., Di Francesco, J., et al. 2021, ApJ, 907, 88
Pattle, K., Lai, S.-P., Hasegawa, T., et al. 2019, ApJ, 880, 27
Pattle, K., Ward-Thompson, D., Berry, D., et al. 2017, ApJ, 846, 122
Pattle, K., Ward-Thompson, D., Hasegawa, T., et al. 2018, ApJL, 860, L6
Pillai, T. G. S., Clemens, D. P., Reissl, S., et al. 2020, NatAs, 4, 1195
Planck Collaboration, Ade, P. A. R., Aghanim, N., et al. 2015, A&A, 576, A104
Planck Collaboration, Ade, P. A. R., Aghanim, N., et al. 2016a, A&A, 586, A138
Planck Collaboration, Ade, P. A. R., Aghanim, N., et al. 2016b, A&A, 586, A136
Punanova, A., Caselli, P., Pineda, J. E., et al. 2018, A&A, 617, A27
Roy, A., André, P., Palmeirim, P., et al. 2014, A&A, 562, A138
Shimajiri, Y., André, P., Palmeirim, P., et al. 2019, A&A, 623, A16
Shu, F. H., Adams, F. C., & Lizano, S. 1987, ARA&A, 25, 23
Soam, A., Pattle, K., Ward-Thompson, D., et al. 2018, ApJ, 861, 65
Sokolov, V., Wang, K., Pineda, J. E., et al. 2018, A&A, 611, L3
Soler, J. D., Alves, F., Boulanger, F., et al. 2016, A&A, 596, A93
Soler, J. D., & Hennebelle, P. 2017, A&A, 607, A2
Stephens, I. W., Looney, L. W., Kwon, W., et al. 2013, ApJL, 769, L15
Stone, J. M., Ostriker, E. C., & Gammie, C. F. 1998, ApJL, 508, L99
Sugitani, K., Nakamura, F., Tamura, M., et al. 2010, ApJ, 716, 299
Tafalla, M., & Hacar, A. 2015, A&A, 574, A104
Tafalla, M., Santiago-García, J., Hacar, A., & Bachiller, R. 2010, A&A, 522, A91
Takakuwa, S., Tsukamoto, Y., Saigo, K., & Saito, M. 2018, ApJ, 865, 51
Tokuda, K., Fujishiro, K., Tachihara, K., et al. 2020, ApJ, 899, 10
Wang, J.-W., Lai, S.-P., Clemens, D. P., et al. 2020, ApJ, 888, 13
Wang, J.-W., Lai, S.-P., Eswaraiah, C., et al. 2019, ApJ, 876, 42
Wang, L.-Y., Shang, H., Su, Y.-N., et al. 2014, ApJ, 780, 49
Ward-Thompson, D., McKee, C. F., Furuya, R., & Tsukamoto, Y. 2020, FrASS, 7, 13
Ward-Thompson, D., Pattle, K., Bastien, P., et al. 2017, ApJ, 842, 66
Wurster, J., & Lewis, B. T. 2020, MNRAS, 495, 3795
Xu, X., Li, D., Dai, Y. S., Goldsmith, P. F., & Fuller, G. A. 2020, ApJ, 898, 122
Yen, H.-W., Koch, P. M., Hull, C. L. H., et al. 2021, ApJ, 907, 33